PONTIFICIA UNIVERSIDAD CATÓLICA DEL PERÚ

ESCUELA DE POSGRADO

A study on the response of the LR-115 detector exposed inside a diffusion chamber and in unconventional bare mode

TESIS PARA OPTAR EL GRADO ACADÉMICO DE DOCTOR EN FÍSICA

AUTOR

Bertin Andrés Pérez Ancaya

ASESORA

Dra. Maria Elena López Herrera

Noviembre, 2021

Declaration

I hereby declare that this dissertation is original and has not been submitted to any institution for assessment purposes. This dissertation is my own work and contains a compendium of publications as a corresponding author or collaborates with others. These publications have been accepteds.

A study on the response of the LR-115 detector exposed inside a diffusion chamber and in unconventional bare mode

Noviembre, 2021

Acknowledgements

This research was supported by the Pontificia Universidad Católica del Perú (PUCP); and founds from CONCYTEC number 236-2015.

I want to acknowledge the supervisor, Dr Maria Elena López Herrera and the co-advisor, Dr Daniel Palacios Fernandez, for their guidance and constant support on the academic aspects. Special thanks go to Dr Antonio Parravicini, Stefano Coria and Francesco Cortesi, who provided laboratory facilities at the Mi.am s.r.l.

Abstract

Several methodologies for radon concentration measurements have been used for monitoring radon in homes and workplaces to minimize health hazards due to indoor radon exposure. One of them is the Nuclear Track Methodology (NTM), commonly used for passive long-term measurements. The LR-115 type II (cellulose nitrate), as an NTM's detector, is often located inside a diffusion chamber. The set formed by the detector and the chamber hereinafter will be called a monitor. Commercial monitors, e.g., *RadOUT*, *Radosys*, *NRPB*, are routinely used for radon measurements; they are calibrated in Certified and/or Accredited Laboratories. However, many laboratories have developed their own monitors, varying some characteristics as geometric shapes, dimensions, and material properties. They also do not have access to calibrate them in Certified and/or Accredited Laboratories. In the present thesis, we studied the detector response given the characteristics of the diffusion chamber that we use, and to know how these characteristics influence radon measurements. The results of this study can provide a fast-calibration of the detector that can be compared to calibrations in Certified and/or Accredited Laboratories. This study is based on Monte Carlo methods that imitate the experimental procedure commonly-used in estimating the calibration factor. This calibration method is more accesible than calibrations performed in Certified and/or Accredited Laboratories due to its low cost, feasibility and applicability. For these purposes, a monitor (LR-115 + a non-commercial diffusion chamber made of polypropylene -usually used as cosmetic pot-) was used in this research. LR-115 detector response in this set-up is reported by taking into account the geometric shape, dimensions and material (conductive or non-conductive) of the chamber, the transmission factor (the ratio of final steady state concentration of radon or thoron at the entrance of the chamber to the concentration of radon or thoron just inside this entrance), radon exposure level, and etching and reading process. Regarding the level of radon exposure, it was possible to correct the track overlap effect for high exposure levels, as can occur in radon measurements in soil pores, by applying a mathematical model. Mainly, these researches show that a non-commercial monitor can work as well as commercial ones. Besides, using an LR-115 in bare mode exposed by unconventional exposition results in concentric ring-shaped tracks, caused by UV natural radiation. The repeatability and reproducibility of the observed phenomenon were experi-

mentally demonstrated. We also studied the ability of the LR-115 detector to register alpha particles from nuclear (n, α) reactions, or radon/thoron progeny. This study is also based on Monte Carlo methods and can provide an estimation of the efficiency of the detector to neutron or radon/thoron progeny.

Table of contents

List of figures

List of tables

Chapter 1

General introduction

1.1 Background information

In the first decade of the twentieth century, particularly in 1911, Ernest Rutherford carried out the gold foil experiment. The experiment consisted of bombarding a sheet of thin gold foil with positively charged alpha particles. He observed that a small number of alpha particles were deflected, which means that Thomson's model could not be accurate. The deflection effect could be explained if the positively charged alpha particle collided with a positive charge. That is the reason why he introduced the idea of a nuclear atom, which contains in its centre a microscopical positively charged nucleus surrounded by planetary electrons [1].

The nucleus is far smaller than the atom and consists of a dense region of protons and neutrons. The proton is positively charged with a mass equal to 1.007276466621u. Simultaneously, the neutron is electrically neutral with a mass equal to 1.00866491595u (https://www.nist.gov/pml/fundamental-physical-constants). Both particles have nearly the same mass and are collectively referred to as nucleons.

If Rutherford's model is accurate, a neutral atom's mass must be equal to its total mass of protons and neutrons. However, the mass of a neutral helium atom is 4.002603u (https://www.nist.gov/pml/fundamental-physical-constants), while the mass of its protons and neutrons as nucleus components is 4.032980u. In other words, the nucleus of the helium atom has approximately 0.030377u less than its components parts. According to Einstein's equation, $E = mc^2$, mass and energy are equivalent. Thus, the difference is mass from the helium atom is equal to a certain amount of energy, called the binding energy. The binding energy is the amount of energy required to separate a nucleus into its components. Fig. 1.1 depicts that iron (^{56}Fe) has the highest binding energy, and nuclides larger than iron show a slight decrease.

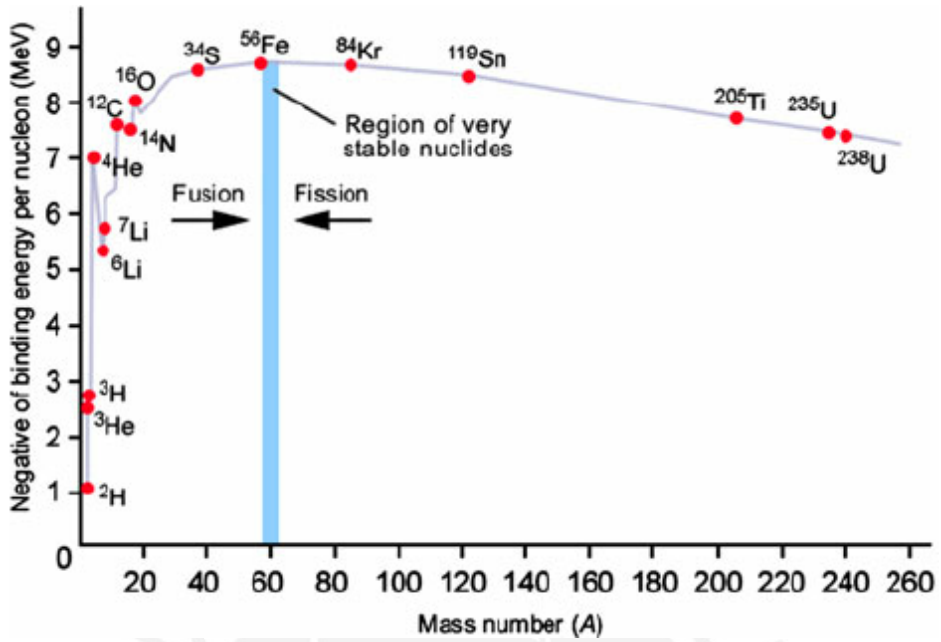

Fig. 1.1 The nuclear binding energy of an isotope and its atomic mass [2].

It is well known that there are four fundamental forces such as the gravitational force, electromagnetic force, weak nuclear force and strong nuclear force. The strong nuclear force is responsible for binding proton and neutrons, described earlier, in a nucleus, while the weak nuclear force is responsible for radioactivity [3].

In radioactivity, there is a conflict between the attractive strong nuclear force and the repulsive electromagnetic force (the electrostatic part), which has implications for the nucleus's stability. Thus, the atomic nucleus would be stable or unstable. For instance, Fig. 1.2 shows that the stable nucleus requires additional neutrons when the number of protons increases to maintain stability. Similarly, Fig. 1.2 also indicates the unstable nuclides categorised by colours (type of decay), such as alpha decay when an unstable nuclide loses two protons and two neutrons. A beta decay when an unstable nuclide emits a beta particle and gamma decay emits high-powered photons (known as gamma rays). As essential extra information, it is easy to see that alpha decay occurs in nuclides with high atomic number.

Alpha decay is a radioactive decay in which an unstable nucleus disintegrates into a more stable nucleus. In the process, the parent nucleus becomes the daughter nucleus by emitting an alpha particle (α). The alpha particle is a heavy, positively charged particle consisting of two protons and two neutrons, commonly referred to as helium nuclei (^4_2He). It has a charge of $+2$, mass equal to 4.001506179127 u (https://physics.nist.gov/cgi-bin/cuu/Value?malul search_for=alpha+particle) and a velocity equal to the twentieth speed of light. Using the

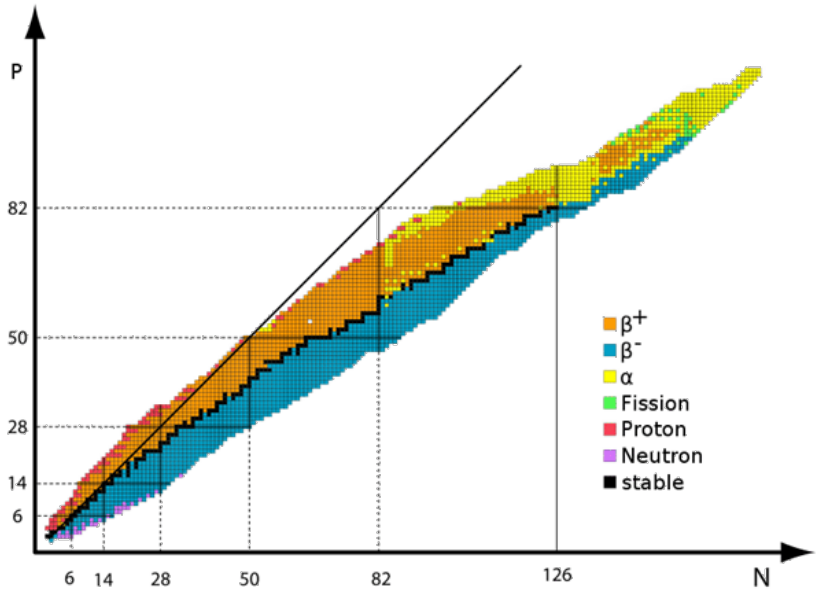

Fig. 1.2 Chart of nuclides represented by their neutrons and protons, the abscissa axis and the ordinate axis, respectively. Black squares represent the stable nuclides, while the coloured squares are unstable nuclides with their respective decay. The continuous line represents, mostly hypothetical, nuclides for which proton number would the same as neutron number. (https://www.geigercounter.org/radioactivity/decay.htm)

alpha particle definition, the general form of alpha decay is

$$ {}^{Z}_{A}X \rightarrow {}^{A-4}_{Z-2}X' + {}^{2}_{4}He^{+2} \tag{1.1} $$

where X is a less stable nucleus called parent, X' is a more stable nucleus, but not completely stable nucleus, called daughter, and ${}^{2}_{4}He^{+2}$ is identical to an alpha particle. Notice that the process of transforming one element (X) to a different one (X') is called transmutation. In alpha decay, the part of the energy involved in alpha disintegration energy (denoted by Q_α) is the sum of the kinetic energies of the alpha particle (KE_α) and the daughter nuclide that recoils $(KE_{daughter})$. The principle of conservation of momentum (product of the mass of alpha particle m_α and its velocity v_α equals to that of the product for daughter nuclide) gives:

$$ m_\alpha \cdot \vec{v_\alpha} = M_{daughter} \cdot \overrightarrow{V_{daughter}} \Longrightarrow \overrightarrow{V_{daughter}} = \frac{m_\alpha}{M_{daughter}} \cdot \vec{v_\alpha} \tag{1.2} $$

This further implies that

$$ Q_\alpha = KE_\alpha + KE_{daughter} = \frac{1}{2}(m_\alpha \mid \vec{v_\alpha} \mid^2) + \frac{1}{2}(M_{daughter} \mid \overrightarrow{V_{daughter}} \mid^2) \tag{1.3} $$

Combining these two equations, the alpha particle's kinetic energy is to be multiplied by a factor equal to $1 + \frac{m_\alpha}{M_{daughter}}$. According to this, there are two energies in alpha decay. One is the energy of the disintegration process. The other is the kinetic energy of the emitted alpha particle, which is slightly less than the energy of disintegration [4].

Transmutations due to alpha decay originate in natural radioactive matter. There are natural occurring nuclides on Earth since the solar system's formation, such as uranium (^{238}U) and thorium (^{232}Th), alpha emitters, and they are called primordial nuclides. Both primordial nuclides are the parents in their decay chains, and it refers to a series of radioactive decays of different radioactive decay product as sequential transmutations. The ^{238}U-chain starts from the unstable parent ^{238}U to the stable daughter lead 206 and the ^{232}Th-chain, from the unstable parent ^{232}Th to the stable daughter lead 208. Both decay chains are shown in Fig. 1.3.

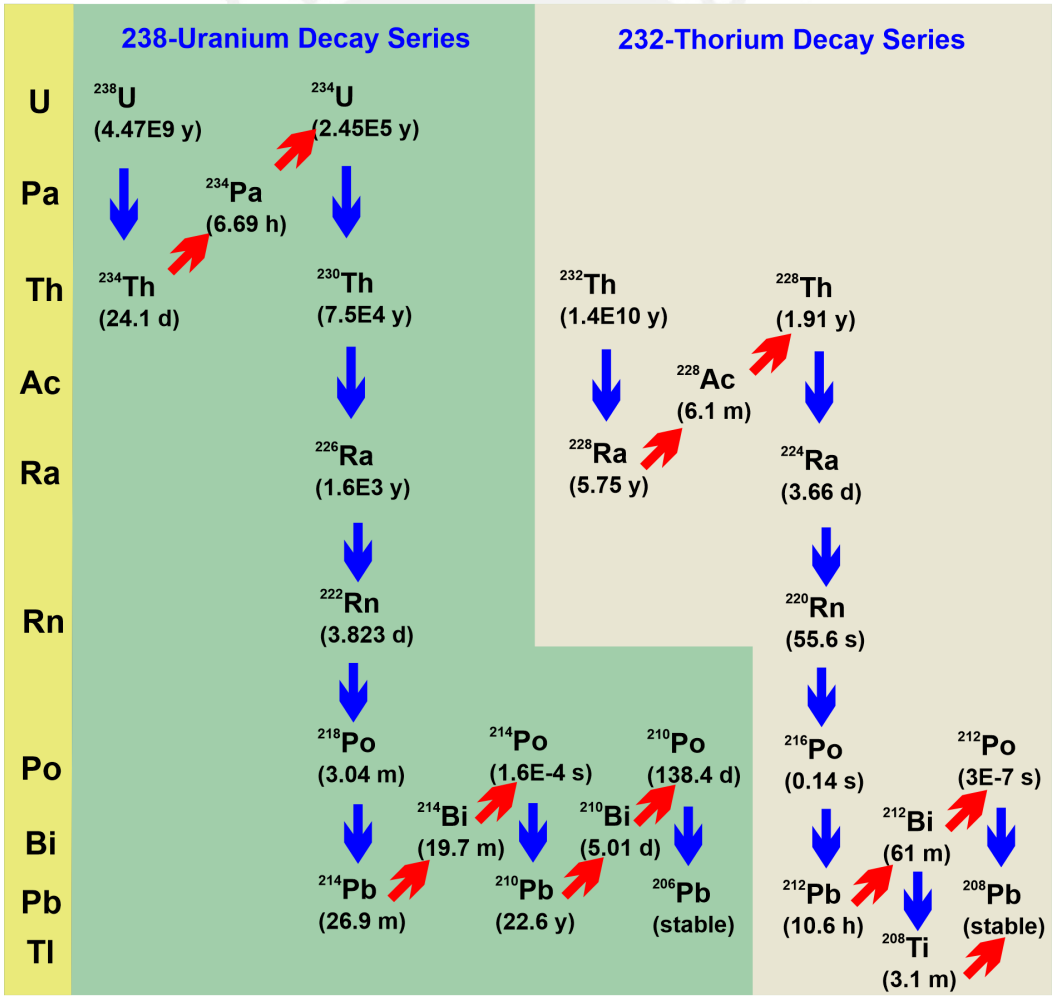

Fig. 1.3 The 238-uranium and 232-thorium decay chains, where blue arrows represent alpha decays and red arrows, beta decays. The images are modified from the decay chains at [5].

Each decay chain has an alpha emitter that has been the subject of this research. The radon (^{222}Rn) comes from uranium decay chain and the thoron (^{220}Rn) from the thorium decay chain. Both are colourless, odourless and tasteless noble gases, and they are naturally present in the soil due to the decay of parents in the earth's crust. The main difference between radon and thoron is that the radon is the most abundant isotope on Earth. Its half-life, defined as the time required for one-half of the atomic nuclei to decay, is relatively less than its isotope thoron.

There is an importance of radon and thoron studies from health-related issues. To be more specific, the radon/thoron progeny is the main contributor to the general population's dose [6]. The inhalation of short-lived progeny are responsible for problems of the respiratory system, lung cancer, and damage to sensitive cells in the skin, as well as causes skin cancer [7–9]

Due to this importance, it makes one wonder how to measure the radon and thoron concentration, because more concentration implies more potential effects or impact. Nowadays, several techniques and instruments are available for radon and thoron measurements and their progeny. A wide range of techniques and apparatus for measuring radon, thoron and their progeny are classified into active and passive, taking into account the duration of the measurement (i.e. seconds or minutes, hours, days and weeks or months) and depending on their physical bases [10].

In active methods, with real-time response, radon samples are obtained by forcing with a pump of a known volume of air or using power supplies. Two measuring instruments are commonly used in various laboratories, these are scintillation cells and ionisation chambers as shown in Fig. 1.4.

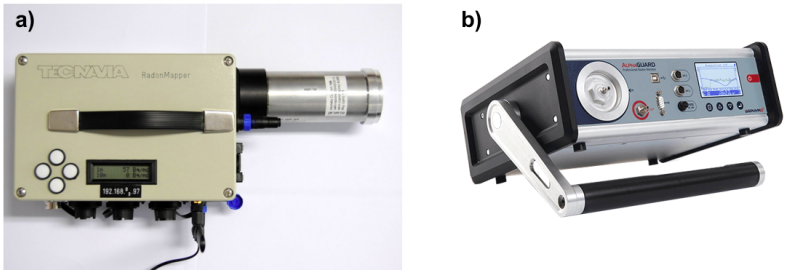

Fig. 1.4 Scintillation cell (Radon Mapper -https://www.miam.it/allegati_catalogo/Radon-Mapper-brochure.pdf-) and ionisation chamber (AlphaGuard -https://www.bertin-instruments.com/product/radon-professional-monitoring/radon-alphaguard/-) as a continuous active device in a) and b), respectively.

Scintillation cells are widely used for grab sample measurements of radon, which usually have a measuring duration of seconds to minutes. A hermetically closed cylinder of stainless

steel, typically called a cell with one end closed by a transparent window and the other end with a single connector is filled with the air of interest by filling through a single vacuum connector. The internal surfaces of the cell are covered with ZnS:Ag (as a scintillator). Alpha particles from radon, thoron or their progeny interact with a scintillator, generating light pulses recorded by a photomultiplier tube and then the generated voltage is recorded by the associated electronics. Several authors have worked with scintillation cells to measure soil gas radon [11], indoor radon [12, 13], radon concentration in drinking water [14, 15] as well as measurements of thoron concentration [16–19]

Ionisation chambers are extensively used as integrator of these gases concentration in air over minutes or hours, repeated indefinitely as continuous active devices. An electrical field is established between an anode and a cathode inside the ionisation chamber. The radon and thoron gases enter, by diffusion mechanism, into the active chamber volume through a glass fibre filter. In the active chamber volume, the current caused by the gas ionisation is generated by the decay of radon, thoron or their progeny. Then alpha particles could be detected or counted separately as pulses by the ionisation chamber, which has a fast response time depending on associated electronics and air replacement rate [20]. Recently, commercial devices based on ionisation chambers have been marketed and adopted as secondary standards in radon calibration laboratories [21]. Several works use devices based on ionisation chamber for soil gas radon concentrations [22, 23], indoor radon [24–26], radon measurements in drinking water [27, 28], thoron measurements [29, 30].

In passive methods, radon samples are obtained by gas's diffusion with no power supplies and no real-time response. Charcoal detectors, electret ion chambers and solid-state nuclear track detectors (SSNTD's) are used as passive detectors as shown in Fig. 1.5. Some of them works as integrator devices.

Fig. 1.5 Charcoal canister (https://www.rtca.com/product.asp?prodID=10&catID=1), electron-ion chambers E-perm (https://radelec.com/store/index.php?-), and solid-state nuclear track detectors (LR-115 on the left side and CR-39 in the right side) in a), b) and c) respectively.

The charcoal canister has activated charcoal, which has an affinity for many gases, including radon/thoron. The granulated activated charcoal is inside the canister with a removable meshed lid. Radon or thoron is retained into the activated charcoal, where radon/thoron progeny will be retained to be measured by gamma spectrometry as well as liquid scintillation counting. In general, charcoal detectors are not true integrators, as the gas absorbed at the beginning of exposure will decay and partially desorb during the exposure. Related to this detectors, several works show how to measure radon/thoron concentrations [31, 32], soil gas radon exhalation [33], indoor radon measurements [34].

Electrets have a permanent surface charge resulting in a surface potential that may be some kV [35]. A set of a conductive plastic chamber and a Teflon electret, which is placed at the bottom of the chamber, is an electret ion chamber (EIC). Radon/thoron gases diffuse into the chamber volume, and the Teflon electret loses charge due to ionisation produced by alpha particles from radon/thoron and their progeny. The EIC is also sensitive to gamma rays, and a correction must be applied. Several works related to this issue have been presented in the literature [36–41].

Some polymers as solid state nuclear track detectors (SSNTDs) can record the alpha particle in form of latent track. In the polymer, its chain breaks due to the interactions of the alpha particle, primary and secondary ionisations occur along its path, forming a latent tracks. Thus, the polymer detectors experience damage due to the breaking chemical bonds [42]. This damage can be visible later by etching the polymer in a NaOH or KOH solution (depending on the type of polymer). LR-115 (cellulose nitrate is the active layer + polyester base is the non-active layer) and CR-39 (poly allyl diglycol carbonate) are used as SSNTDs. These detectors can be used in two modes, such as chamber mode [43] and bare mode [44].

In chamber mode, the detector is placed inside a diffusion chamber where the diffusion is the main transport mechanism for radon/thoron to reach the internal volume of the diffusion chamber. In such a case, the entry of radon/thoron into the detection volume of a diffusion chamber is attenuated by a diffusive or permeation barrier. In this mode, a set formed by the diffusion chamber and a detector is called monitor. There are commercial monitors that are widely used by many laboratories, however other laboratories have developed and use their own non-commercial monitors. These monitors should be calibrated using some primary or secondary standard system [45]. Nevertheless, these systems are not fully accesible to some laboratories. That is why the calibration can also be stablished by using methods that are based on Monte Carlo simulations [46–49]. This simulations take into account several characteristics of the diffusion chamber, the detector and the level of radon/thoron exposures, and can be comparable when using a primary or secondary standard system.

When detectors are exposed to high levels of radon concentration, there is an effect called overlapping [50–52], which will be also taking into account in this work.

In bare mode, the detectors are also used to indirectly register radon/thoron progeny or neutrons [53–56]. In these references, the authors use a specific film covered detector, depending on which alpha particle they want, either nuclear (n, α) reactions or radon/thoron progeny. For instance, an absorber film covered detector -such as mylar aluminized- are able to rearrange the energy detection range in order to register alpha particles from radon/thoron progeny in the detector. Also, a converter film covered detector -such as boron converters- are able to create alpha particles due to the nuclear (n, α) reaction. Both cases were studied by using Monte Carlo methods to estimate the efficiency of the detector.

1.2 Research aims and objectives

1.2.1 Main objectives

This thesis aimed to study the response of an LR-115 detector exposed inside a diffusion chamber and in unconventional bare mode.

- To study LR-115 detectors exposed inside a diffusion chamber is based on simulations and comparisons between experimental and simulated results. The developed simulation method could be a more accessible way to estimate the detector response compared to conventional calibration using primary or secondary standards.
- To apply all possible parameters-such as the geometric shape, dimensions and material of the chamber, the transmission factor, radon exposure level, and etching and reading process-in simulations that may influence the LR-115 response to get simulation results in good agreement with the experimental outcomes.
- Detectors will be exposed in bare mode to understand how an unconventional mode of exposure leads to registration of concentric rings in etched detectors due to ambient UV radiation.

1.2.2 Specific objectives

The specific objectives of this thesis are:

- Determine the radon/thoron transmission factor in a cylindrical diffusion chamber in order to estimated the real concentration inside the diffusion chamber.

- Estimate the calibration factor of an LR-115 detector inside a non-commercial-conductive cylindrical diffusion chamber using Monte Carlo methods.
- Evaluate the likely influence of the type of the chamber's material in the calibration factor or detector response.
- Examine the impact of the track overlapping effect on detectors exposed to high levels of radon concentration, and develop a model that could fix the influence of the track overlapping effect on a non-commercial monitor (cylindrical diffusion chamber + LR-115) that can be used with other chambers and different experimental parameters.
- Investigate how a concentric ring track is formed in a detector by exposing the bare detector to unconventional exposition.
- Examine the influence of the UV natural radiation when irradiating a bare LR-115 to unconventional exposition.
- Show a brief discussion of how the used methodology to study the detector response can be applied to detectors covered by converters or absorbers, normally used to register alpha particles from nuclear (n, α) reactions or radon/thoron progeny, respectively.

Chapter 2

LR-115 detector exposed inside a diffusion chamber

2.1 LR-115 detector response for short and long term exposures

When an LR-115 detector is exposed to radon inside a diffusion chamber, it registers alpha particles emitted in radon's decay and its progeny [43]. In this work, the arrangement used in the calculations was a cylindrical diffusion chamber (CDC) made of a non-conductive material in which the entry of radioactive gas occurs through the thread between cylinder and cover. Several features for calculating the detector response are presented below.

2.1.1 Radon/Thoron transmission factor

A diffusion chamber for radon measurements is commonly used to reduce the entry of dust, the entry of radon/thoron progeny and to reduce the presence of thoron in the detection volume. The latter is because the half-life of thoron is too short to travel trough the entire thread before decaying. During radon measurements, radon gas reaches the internal volume by diffusion, which is the primary transport mechanism. The radon gas typically enters the chamber through a membrane [57], pin-holes [58], gaps [59] or threads [60]. These types of entries do also not allow 100% of radon gas to enter the internal volume. The radon transmission factor allows estimating the percentage of entry in the internal volume, assuming that the effect of turbulence is minimized by taking into account reasonably small entries. This factor is the ratio of the final steady-state concentration to the initial concentration (just outside the entries).

According to [58], the non-steady state equation for the radon concentration $C(t)$ inside the diffusion chamber at a time equal t can be written as the following equation:

$$\frac{\partial C(t)}{\partial t} = J\frac{A_i}{V_{CDC}} - \lambda_i C(t) \tag{2.1}$$

where J is the flux through the type of entry, $V_{CDC}(cm^3)$ is the volume of the diffusion chamber, $A_i(cm^2)$ is the area of the entry type and λ_i is the decay constant of radon or thoron gas. Applying Fick's diffusion law, the flux J is proportional to the difference between outside and inside gas concentration. In this context, the membrane flux (J_m), the pin-hole flux (J_{ph}), the gap flux (J_g) and the thread flux (J_t) can be expressed as follows:

$$\begin{aligned} J_m &= \frac{K(C_o - C(t))}{d_m} \\ J_{ph} &= \frac{D(C_o - C(t))}{d_{ph}} \\ J_g &= \frac{D(C_o - C(t))}{d_g} \\ J_t &= \frac{D(C_o - C(t))}{d_t} \end{aligned} \tag{2.2}$$

where C_o is the initial concentration just outside the entry, K is the membrane permeability coefficient, D is the diffusion coefficient, d_m is the thickness of the membrane, d_{ph} is the thickness of the pin-hole, d_g is the thickness of the gap, and d_t is the total distance that the gas travels through threads. The flux expression depends on the types of entry and can be replaced in Eq. (2.1). Using the thread flux, we arrive at

$$\frac{\partial C(t)}{\partial t} = \left(\frac{D}{d_t}\frac{A_i}{V_{CDC}}\right)C_o - \left(\frac{D}{d_t}\frac{A_i}{V_{CDC}} + \lambda_i\right)C(t) \tag{2.3}$$

In general, Eq. (2.3) depends on an initial condition, such as $C(t=0)=0$. So the solution is given by

$$C(t) = C_o\left(\frac{\frac{A_i D}{V_{CDC}d_t}}{\lambda_i + \frac{A_i D}{V_{CDC}d_t}}\right)\left(1 - \exp^{-\left(\lambda_i + \frac{A_i D}{V_{CDC}d_t}\right)t}\right) \tag{2.4}$$

At large times, a steady-state concentration (C_s) is reached in the internal volume. Rewriting the Eq. (2.4) with $\lim_{t\to\infty}(1-\exp^{-at}) = 1$, the C_s concentration is found to be:

$$C_s = C_o\left(\frac{\frac{A_i D}{V_{CDC}d_t}}{\lambda_i + \frac{A_i D}{V_{CDC}d_t}}\right) \tag{2.5}$$

As defined above, the transmission factor (F) is equal to C_s/C_o, as well as [58] reported:

$$F = \frac{\frac{A_i D}{V_{CDC} d_t}}{\lambda_i + \frac{A_i D}{V_{CDC} d_t}} \tag{2.6}$$

In this particular case, A_t corresponds to the lateral area formed between the screw cap and the chamber.

Using the Eq. (2.4), the transmission of radon $(\lambda_{rn} = 1.259 \times 10^{-4} min^{-1})$ and thoron $(\lambda_t = 7.453 \times 10^{-1} min^{-1})$ into a CDC ($r_{CDC} = 3cm$ and $h_{CDC} = 4cm$) with $D = 0.1 cm^2/s$, $A_t = 0.13 cm^2$, $d_t = 2.77 cm$ and $V_{CDC} = 113.097 cm^3$ is shown in Fig. 2.1.

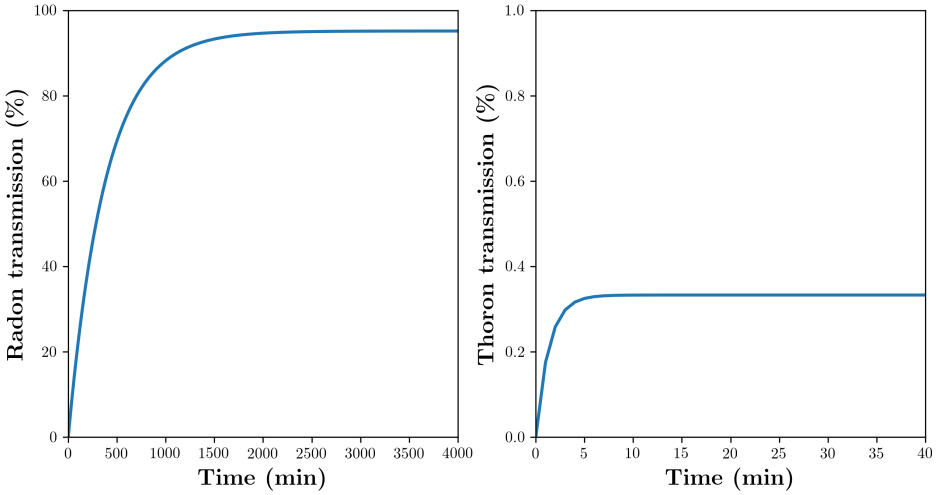

Fig. 2.1 Temporal response of radon and thoron transmission into a CDC.

Fig. 2.1 depicts that this chamber prevents 99.67% of thoron gas ingress. As mentioned above, the thread entry allows 95.19% of radon gas into the internal volume.

2.1.2 Travelling distance of alpha particles

When radon gas enters the chamber, it decays into its progeny. Radon and its progeny emit alpha particles with different kinetic energies, as shown in Table. 2.1.

Table 2.1 Kinetic energy of an alpha particle emitted by radon or its progeny.

Nuclides	Alpha particle kinetic energy$[keV]$
Radon	5489.48
^{218}Po	6002.35
^{214}Po	7686.82

These alpha particles travel in the internal air of the chamber. In this context, air density (ρ_a) plays an essential role in the alpha particle range in air and can be calculated as follows [61].

$$\rho_a = \frac{0.34848 \cdot p - 0.009024 \cdot H_r \cdot \exp^{0.0612 \cdot T}}{273.15 + T} \tag{2.7}$$

where p is the barometric pressure (hPa), H_r is the air humidity $(\%)$ and T is the air temperature $(^{\circ}C)$. To estimate an alpha particle's travelling distance, we first calculate its stopping power with energies from 0.01 to $10.00MeV$ and a specific air density $(1.20484kg/m^3)$. The stopping power (dE/dx) can be calculated using the SRIM-2013 program [62], as shown in Table. 2.2.

Table 2.2 Stopping power of alpha particles in air obtained from SRIM-2013.

Ion Energy [MeV]	Total dE/dx $[\frac{MeV}{mm}]$	
	dE/dx Electronic	dE/dx Nuclear
0.0100	3.82E-02	7.36E-03
0.0550	8.96E-02	2.46E-03
0.0700	1.01E-01	2.06E-03
0.0900	1.14E-01	1.71E-03
0.1700	1.55E-01	1.05E-03
0.3250	2.04E-01	6.26E-04
0.5000	2.31E-01	4.40E-04
0.7000	2.39E-01	3.33E-04
1.0000	2.28E-01	2.47E-04
1.2000	2.15E-01	2.11E-04
1.6000	1.88E-01	1.65E-04
1.8000	1.77E-01	1.50E-04
2.0000	1.66E-01	1.37E-04
5.0000	9.26E-02	6.16E-05
8.0000	6.59E-02	4.07E-05
10.0000	5.62E-02	3.34E-05

By integrating the stopping power, the travelling distance of an alpha particle is calculated as follows:

$$d_{air} = \int_{E_o}^{E_i} \frac{1}{dE/dx} \tag{2.8}$$

where E_o is the initial energy of an alpha particle, and E_i is the energy of an alpha particle after travelling a distance d_{air}. Eq. (2.8) can be calculated by numerical methods, as shown in Appendix A. Then, the travelling distance curve for an alpha particle emitted by radon ($E_o = 5.48948 MeV$) is graphically illustrated in Fig. 2.2.

Fig. 2.2 also depicts that an alpha particle emitted by radon travels cm in the air when it loses half its energy, and it travels cm in the air when it loses all its energy. Similarly, the travelling distance curve for alpha particles emitted by radon progeny is also calculated and showed in Fig. 2.3.

At this point, the dependence of the air density in this curve is still needed. We applied the same calculations for different air densities to estimate a family travelling distance curve for

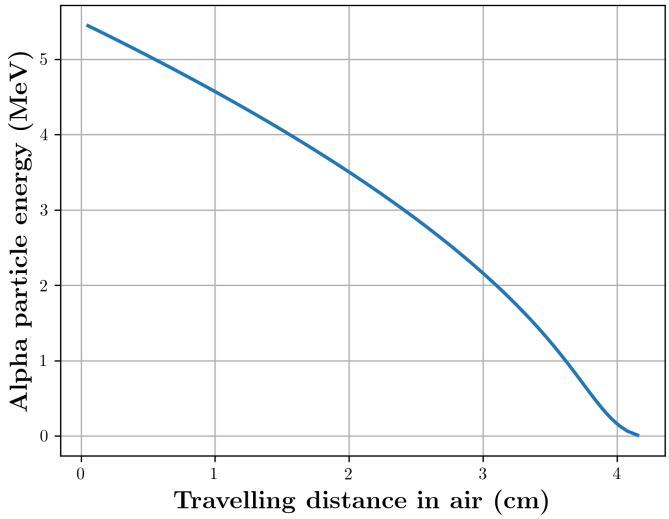

Fig. 2.2 Radon alpha particle energy as a function of distance traveled in air.

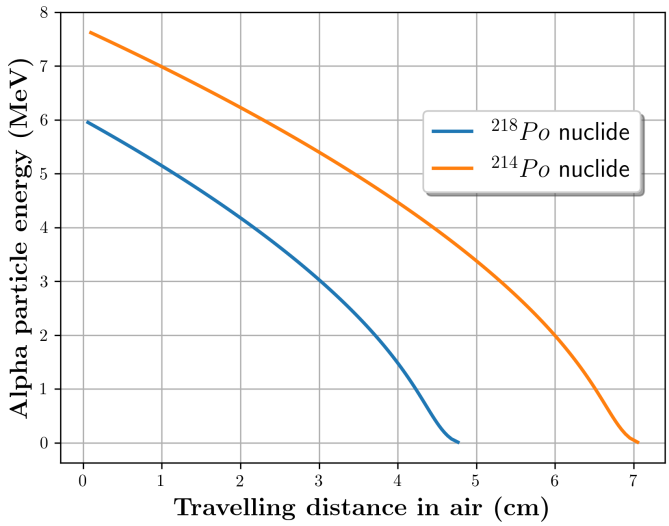

Fig. 2.3 Radon progeny alpha particle energy as a function of distance traveled in air.

radon and its progeny products. The family curves for these nuclides are shown in Fig. 2.4, Fig. 2.5 and Fig. 2.6.

These family curves come in handy to define the detection distance limits into the chamber's internal volume combined with the given energy window. We can compute the minimum and the maximum detection distances by replacing in Eq. (2.8) the maximum and the minimum limits of the energy window, respectively.

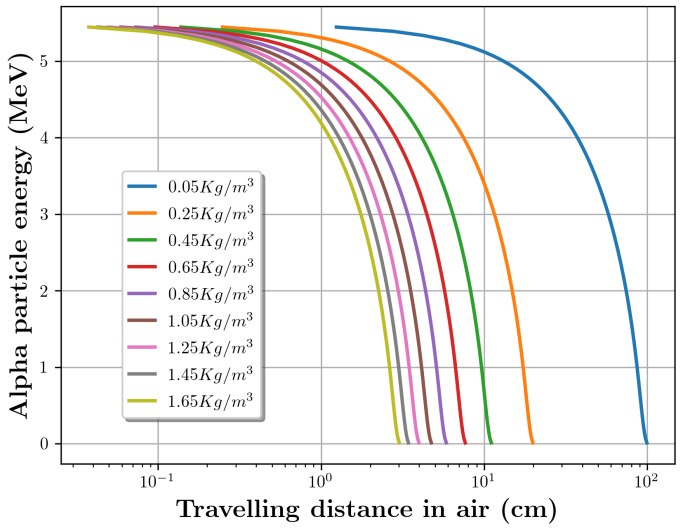

Fig. 2.4 Radon alpha particle energy as a function of distance traveled in different air densities.

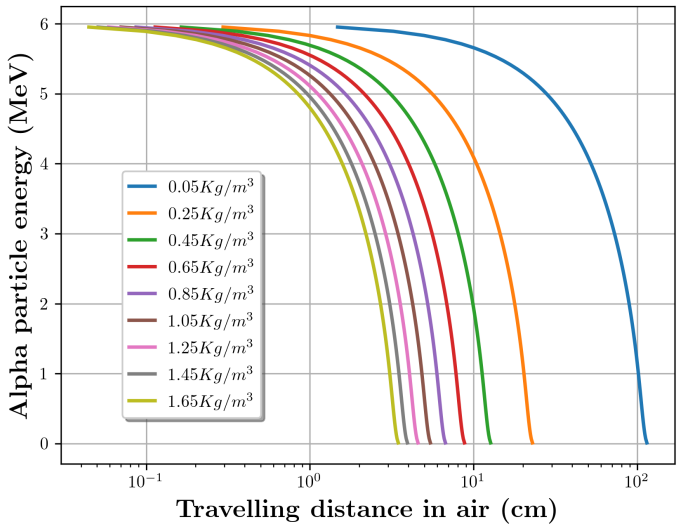

Fig. 2.5 ^{218}Po alpha particle energy as a function of distance traveled in different air densities.

2.1.3 Energy window of the LR-115 detector

LR-115 detectors register alpha particles with energies within the energy window, generating visible tracks on the active layer of the detector. The energy window of the LR-115 is $[0.8-4.5]MeV$ when detectors are chemically etched in in $2.5N\ NaOH$ solution at $60^{\circ}C$

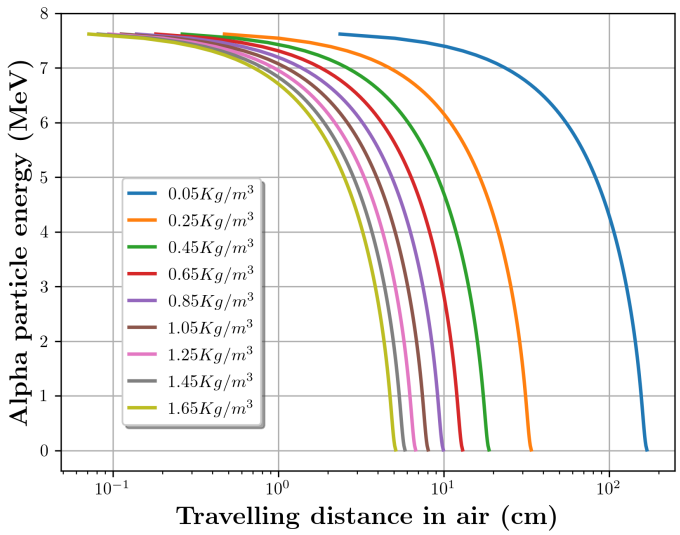

Fig. 2.6 ^{214}Po alpha particle energy as a function of distance traveled in different air densities.

for 90 minutes considering $v_B = 3.27\mu m/h$, according to the manufacture specifications (http://www.gt-analytic.at/downloads_en/Kod_tech_det.pdf).

The energy window strongly depends on the parameters such as the etching condition, adopted visibility and the V function. During etching process, etched tracks in the LR-115 detector are modelled by the V function. This function is of the form $V = V_t/V_b$, where V_t is the track etch rate where the etching goes along the particle path, and V_b is the bulk etch rate where the etching progresses in all directions on the active layer of the detector. Four different V functions, where their constants were experimentally obtained by some authors, are shown in Table. 2.3.

Table 2.3 Four V functions obtained by different authors.

	Reference	V function
A	[63]	$V = 1 + \left(100e^{-0.446R} + 4e^{-0.044R}\right)\left(1 - e^{-R}\right)$
B	[64]	$V = 1 + \left(100e^{-0.446R} + 5e^{-0.107R}\right)\left(1 - e^{-R}\right)$
C	[65]	$V = 1 + \frac{1}{\left(0.23^2 + \left(0.032^2 R - \frac{1}{3.8^2 R}\right)\right)\cdot 3.27}$
D	[66]	$V = 1 + \left(14.23e^{-0.48R} + 5.9e^{-0.077R}\right)\left(1 - e^{-R}\right)$

It is essential to mention that any V function can not be the best description of the experimental processes, because this function is an empirical function. Each V function was

derived using different experimental parameters that calculate the V function's constants. Function A[63] and B[64] were derived using the concentration of the $NaOH$ solution from the etching process as an experimental parameter. Function C[65] was derived using two different approaches, V_t was correlated with the alpha particle energy or with the ionization velocity, while the function D[65] was derived using the track density. The visibility criterion was set as a completely perforated track, with major and minor axes of the visible bottom track openings not less than $1\mu m$.

Considering these three parameters, we can compute the energy window using the $TRACK\_TEST$ code [67]. A Python subroutine was written to estimate the energy window, and this subroutine iterates several incident angles for each incident energy using the $TRACK\_TEST$ code. The subroutine reads the input parameters, such as the V function, etching time, V_b value and the visibility criterion. Generally, the $TRACK\_TEST$ code returns the $Output\_3D.dat$ file, which gives the coordinates of points on the track wall in three dimensions. The subroutine uses this file to identify the major and minor axes of the top and bottom perforations (Fig. 2.7) formed in the active layer of the LR-115 detector.

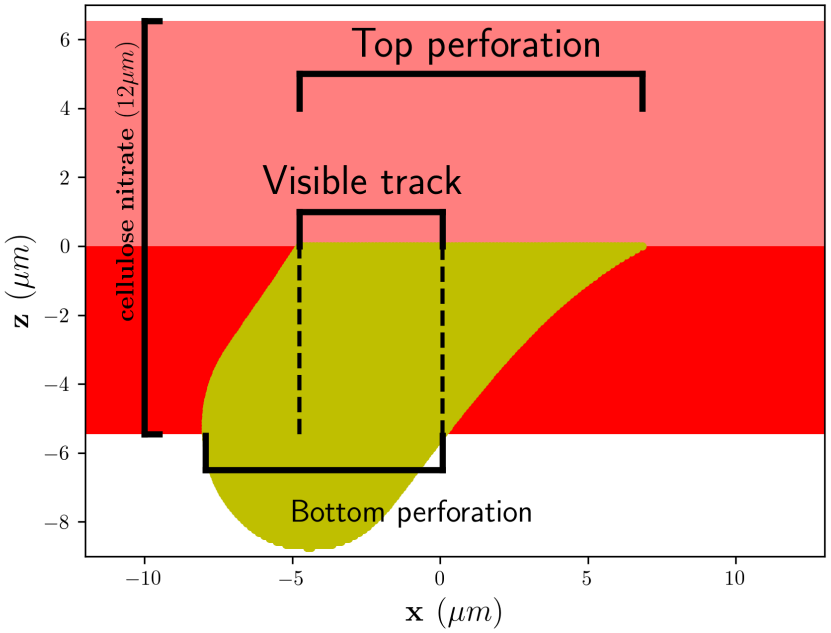

Fig. 2.7 Track formation during etching treatment.

By applying a geometric Python algorithm, it is possible to estimate the axes of the visible bottom track openings (referred as visible track in Fig. 2.7). If these axes are greater than $1\mu m$, the incident energy (E_x) and incident angle (θ_x) are stored. In this case, E_x and θ_x

values can generate a visible track. The minimum incident angle of an alpha particle that produces a visible track (meets the visible criterion condition) was stored and called the critical angle. According to mentioned above, we can say that the critical angle is related to the incident energy, as shown in Fig. 2.8.

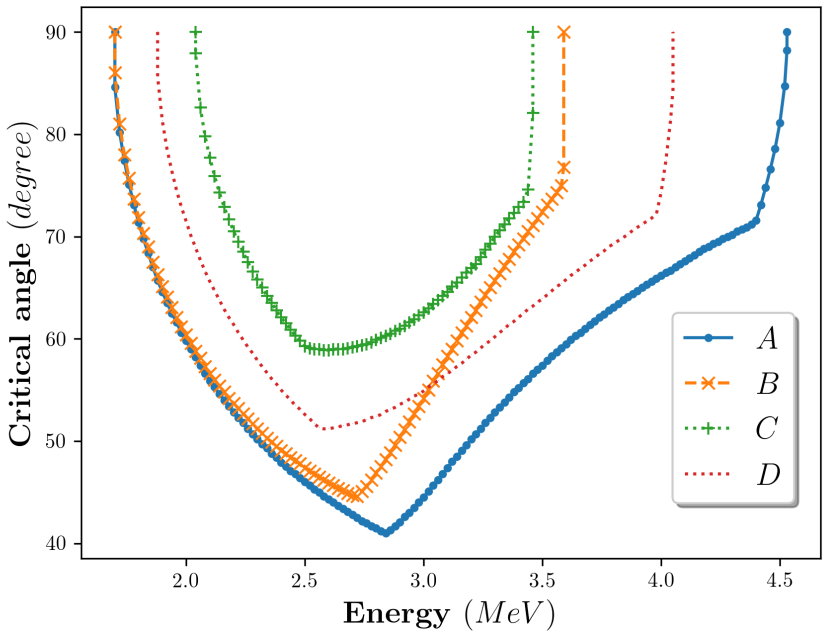

Fig. 2.8 Critical angle-energy curves for LR-115 using the V functions indicated with A, B, C and D in Table. 2.3.

Fig. 2.8 depicts the relation between critical angle and incident energy for the four different functions. The $(E_x,)\theta_x$ values within the area between the critical angle-energy curve and the critical angle value equal to 90 meet the conditions that allow generating visible tracks, while with outer values do not generate visible track after an etching process.

2.1.4 Partial sensitivity to radon

In this section, the partial sensitivity to radon of the LR-115 detector inside a CDC is calculated. The partial sensitivity is defined as the product of the geometric efficiency (ε_g) and the intrinsic efficiency (ε_i). The geometric efficiency is related to the fraction of alpha particles that are directed towards the detector $(N_{h,air})$ over the total of alpha particles, that hit the detector with a non-zero probability, emitted from a certain volume $V_{h,air}[cm^3]$ of air in front of the detector, so it is mathematically expressed as $\frac{V_{h,air}}{\pi r_d^2}$, where $r_d[cm]$ is the

radius of the detector. On the other hand, the intrinsic efficiency is related to estimating how many alpha particles directed towards the detector are registered by the detector, or considered visible tracks, so it is mathematically expressed as $\frac{N_{v,air}}{N_{h,air}}$, where $N_{v,air}$ is the number of registered alpha particles. Using both variables, the partial sensitivity $(S_{i,air}[cm])$ can be defined as follows:

$$S_{i,air} = \frac{N_{v,air}}{N_{h,air}} \cdot \frac{V_{h,air}}{\pi r_d^2} \tag{2.9}$$

In Eq. (2.9) , $V_{h,air}$ term can be expressed in terms of V_{CDC} and the total number of alpha particles from the entire V_{CDC} volume $(N_{t,air})$

$$V_{h,air} = \frac{V_{CDC} \cdot N_{h,air}}{N_{t,air}} \tag{2.10}$$

Replacing Eq. (2.10) into Eq. (2.9), we obtain a simplified expression for the partial sensitivity to radon

$$S_{i,air} = \frac{N_{v,air}}{N_{t,air}} \cdot \frac{V_{CDC}}{\pi r_d^2} \tag{2.11}$$

Monte Carlo simulation was used to estimate this partial sensitivity. This simulation is a fictitious representation of reality that uses many random numbers to obtain numerical results. Random numbers use unpredictable physical means to generate numbers, while pseudo-random numbers use mathematical algorithms. Several research types have been done on radon numbers, insomuch that the modern algorithm used for pseudo-random number generators produce sequences that reliably imitate truly random sequence [68–70]. For these reasons, we use pseudo-random numbers from Python modules, where there is a basic function called $random()$. This function generates pseudo-radon numbers of $53-bit$ precision floats and a period of $2^{19937}-1$.

The partial sensitivity can be computed by two simulations (A and B) concerning the Monte Carlo simulation. Simulation A mimics how detectors inside a CDC are exposed to different radon exposures, just like radon calibration laboratories do [71], in order to get more realistic uncertainties. Simulation B is the typical Monte Carlo simulation that depends on the amount of sampled random numbers to improve the uncertainty's statistic [46–49].

Both simulations start sampling the total positions of alpha particles emitted by radon in the air state into the CDC. On the one hand, simulation A samples an $N_{t,air,A} = V_{CDC} \cdot E_{rn} \cdot 3.6$ positions, where E_{rn} is the radon exposure in $kBqh/m^3$. On the other hand, simulation B samples $N_{t,air,B} = 10^9$ positions. These positions are randomly sampled using cylindrical

coordinates (r_1, θ_1, z_1):

$$\begin{aligned} r_1 &= r_{CDC}\sqrt{\xi_1} \\ \theta_1 &= 2\pi\xi_2 \\ z_1 &= h_{CDC} \cdot \xi_3 \end{aligned} \tag{2.12}$$

where ξ_1, ξ_2 and ξ_3 are random uniform numbers between 0 and 1. Then, $N_{v,air}$ is estimated via rejection technique. In this process, the number of alpha particles from $N_{t,air,A}$ or $N_{t,air,B}$ that generates visible tracks is selected with the above conditions. Finally, we can replace parameters obtained from simulations into Eq. (2.11) to estimate the partial sensitivity to radon. For instance, Appendix A shows how to do that using some Python recipes.

2.1.5 Partial sensitivities to radon progeny

In this section, we can calculate the partial sensitivity to radon progeny of the LR-115 detector inside a CDC. Unlike radon behaviour, the radon progeny decay in two states into the CDC. ^{218}Po atoms decay in both air and deposited state, while ^{214}Po atoms almost fully decay in the deposited state [72]. In other words, f_1 fraction of ^{218}Po atoms emit alpha particles from the air, $1 - f_1$ fraction emits from walls of CDC, and all ^{214}Po atoms emit alpha particles from walls of CDC. This behaviour of ^{214}Po is because its parent ^{214}Pb has a high probability to be in the deposited state due to its long half-life $(t_{1/2} = 26.8min)$. The partial sensitivity to ^{218}Po in air state is estimated in the same ways as assessed for radon, however the partial sensitivity in deposited state $(S_{i,wall})[cm]$ changes considering the internal walls of the chamber. In such a case, Eq. (2.11) change to Eq. (2.13).

$$S_{i,wall} = \frac{N_{s,wall}}{N_{t,wall}} \cdot \frac{S_{CDC}}{\pi r_d^2} \cdot \frac{V_{CDC}}{A_{CDC}} \tag{2.13}$$

where $S_{CDC}[cm^2]$ is the total internal surface area of the CDC, $N_{s,wall}$ is the number of alpha particles that generates visible tracks from S_{CDC}, $N_{t,wall}$ is the total number of alpha particles from S_{CDC}, and A_{CDC}/V_{CDC} was added to normalize the units to cm. In this case, positions are randomly sampled into two sections, lateral walls and upper walls. For lateral walls, the positions are

$$\begin{aligned} r_2 &= r_{CDC} \\ \theta_2 &= 2\pi\xi_4 \\ z_2 &= h_{CDC} \cdot \xi_5 \end{aligned} \tag{2.14}$$

where ξ_4 and ξ_5 are random uniform numbers between 0 and 1. Similarly, for upper walls, the positions are

$$\begin{aligned} r_3 &= r_{CDC}\sqrt{\xi_6} \\ \theta_3 &= 2\pi\xi_7 \\ z_3 &= h_{CDC} \end{aligned} \tag{2.15}$$

where ξ_6 and ξ_7 are random uniform numbers between 0 and 1. Finally, the partial sensitivity to radon progeny is the sum of the partial sensitivity to radon progeny for deposited progeny on lateral and upper walls ($S_{i,wall} = S_{i,wall,lateral} + S_{i,wall,upper}$). So each partial sensitivity is estimated as similar as Section (2.1.4), but using equation Eq. (2.13) and taking into account the lateral

2.1.6 The airborne fraction of ^{218}Po atoms

It is well known that the ^{218}Po atoms decay into two states [72, 73]. So it is essential to know the f_1 fraction value and differentiate how many ^{218}Po atoms decay into air state and deposited state. It is a necessary parameter that we will use later to calculate the total sensitivity, or similarly, the detector response, because the total sensitivity also depends on the f_1 fraction. This fraction has been evaluated in various studies. For instance, f_1 is less than 0.5 [74–76]. According to [77], f_1 can vary from 0.04 to 0.4. A similar finding of f_1 values ~ 0.5 was obtained by [66] using the LR- 115 detectors inside a diffusion chamber. They usually use conductive diffusion chambers.

Besides, the atoms -such as ^{218}Po and ^{214}Po- deposited on the inner walls of the diffusion chamber must follow a certain distribution. The type of distribution can influence the value of f_1. Some authors assume a uniform deposition when estimating the detector response [78, 48]. However, in [72], the distribution of the deposited atoms is assumed not uniform and f_1 will exceed up to 0.23. The non uniform distribution is also shown by [79].

According to information from previous reference, we must determine the radon progeny distribution onto the chamber walls because this can influence the value of the f_1 fraction. ^{218}Po and ^{214}Po are positively charged atoms immediately after formation. These atoms in the presence of an electric field behave differently compared to an electric field equal to zero, and this difference can be an important factor when estimating the type of distribution of the deposited atoms. Given this difference, the CDC's material can also affect this distribution because, in general, this material can be conductive or non-conductive.

A conductive CDC works as a Faraday cage. This cage operates because an external electric field can cause some electric charges within CDC material to be distributed to cancel the field's effect in the interior CDC. In other words, the electric field inside a conductive

CDC is equal to zero. On the other hand, the electric charges in a non-conductive CDC do not have a chance to rearrange as they are fixed, so the electric field inside a non-conductive CDC is not equal to zero.

We can explore the relationship between the radon progeny distribution and the CDC's material using the stochastic Langevin's equation [80–82]. This equation is a stochastic differential equation describing the time evolution of the spatial distribution of radon progeny, particularly ^{218}Po deposited atoms, in the CDC's internal surface. As noted above, for a conductive CDC, F_{ext} is equal to zero, while a non-conductive CDC, an additional F_{ext} force, caused by Coulomb force, is needed.

$$m\frac{d^2}{dt^2}x(t) = -m\eta\frac{d}{dt}x(t) + F_{ext}(x) + m\zeta(t) \tag{2.16}$$

where $x(t)$ is the time-dependence of the position, m mass of the particle, η is the friction coefficient, and ζ is the stochastic term.

A significant quantity of radon progeny atoms will continuously collide with one another or/and air molecules in the CDC's internal volume. So the friction term, therefore, is expected to contribute rather than the inertial term. It means that the inertial concept can be ignored, neglecting the inertial terms of Eq. (2.16). We obtain

$$\frac{d}{dt}x(t) = \frac{F_{ext}(x)}{m\eta} + \frac{\zeta(t)}{\eta} \tag{2.17}$$

We solve Eq. (2.17) using the following expression reported by [83]:

$$x_t = x_{(t=0)} + \frac{Dt}{k_B T}F_{ext} + \sqrt{(2Dt)}\cdot g \tag{2.18}$$

where t is the numerical time-step, $x(t=0)$ is the initial position of a radon progeny product atom, x_t is the final position at t equal to $-\tau\cdot\ln(1-\xi_8)$ (τ is the mean lifetime, and ξ_8 is a uniform random number between 0 to 1, [72]), $D = 0.054cm^2/s$ is the diffusion coefficient as well as [84] and [73] used in their calculations, k_B is the Boltzman constant, T is the temperature, and g symbolizes a Gaussian distribution of zero mean and unit variance. At this point, Gaussian random numbers can be sampled by the Box-Muller transform [85] as shown as follows:

$$g = \sqrt{(-2\cdot\ln\xi_9)}\cdot\cos(2\pi\cdot\xi_{10}) \tag{2.19}$$

where ξ_9 and ξ_{10} are uniform random number between 0 to 1. This transformation is a sampling method for generating pairs of uniform random numbers and transform them into Gaussian random numbers.

We studied a conductive and non-conductive chamber. In conductive chamber we replaced the external force equal to zero in Eq. (2.18), while an external force, that is generated by the electric field between a charged ion and the charge induced in the chamber (according to [72]) was applied in Eq. (2.18). Then, Gaussian random numbers were sampled by writing a Python algorithm using the Eq. (2.19) and the function $random.uniform(0,1)$. For our study, we used a cylindrical chamber with radius $r_{CDC} = 3cm$ and hight $h_{CDC} = 4cm$ for both conductive and non-conductive chamber. Finally, the Eq. (2.18) was computed in Python using all the above parameters and we obtain results for conductive and non-conductive chamber as shown in Fig. 2.9 and Fig. 2.10, respectively.

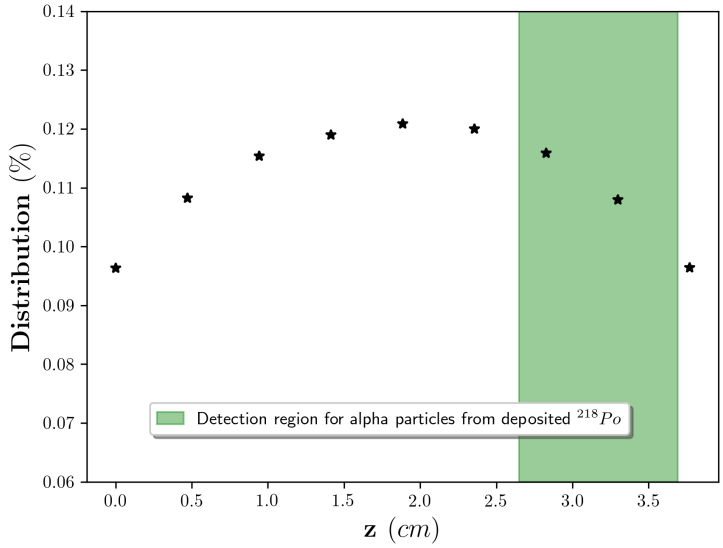

Fig. 2.9 Distribution of deposited ^{218}Po along the internal wall of a conductive chamber. The green zone is the detection region for alpha particles from deposited ^{218}Po that generate visible tracks.

Fig. 2.9 and Fig. 2.10 depict that the deposited ^{218}Po atoms distributions are slightly similar, principally at the detection region. Similar results are obtained in [72] with different values due to the stochastic nature of the equation but similar in curved-shape. Being thorough in numerical results, the non-conductive CDC registers 0.39% more alpha particles emitted by deposited ^{218}Po atoms than the conductive one. In terms of the f_1 fraction, this value for a non-conductive CDC is slightly smaller than a conductive one because more deposited ^{218}Po atoms mean more non-deposited ^{218}Po (air state). Due to the small variation we can say that the importance of the material is not significant.

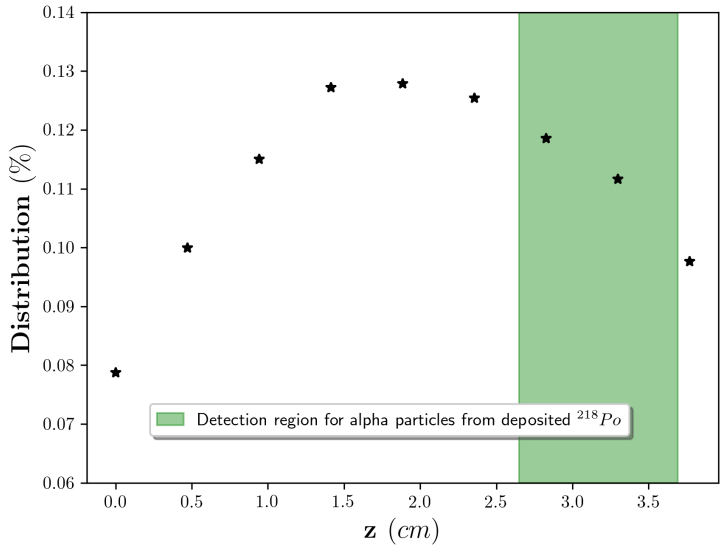

Fig. 2.10 Distribution of deposited ^{218}Po along the internal wall of a non-conductive chamber. The green zone is the detection region for alpha particles from deposited ^{218}Po that generate visible tracks.

2.1.7 Total sensitivity

The total sensitivity of the LR-115 is equivalent to the sum of the partial sensitivities taking into account the features above:

$$S_{total} = S_{radon,air} + (f_1)S_{^{218}Po,air} + (k_{lateral})(1-f_1)S_{^{218}Po,wall,lateral} + (k_{upper})(1-f_1)S_{^{218}Po,wall,upper} + (k_{lateral})S_{^{214}Po,wall,lateral} + (k_{upper})S_{^{214}Po,wall,upper} \quad (2.20)$$

where the $k_{lateral}$ and k_{upper} is proportional to the total area of the lateral and upper internal walls of the chamber, respectively, the subscript i from Eq. (2.11) and Eq. (2.13) can be *radon*, ^{218}Po and ^{214}Po. As an example, the total sensitivity of the LR-115 inside the CDC is estimated using both simulations A and B. Each simulation uses five different V functions to find that best describe a real experiment.

First of all, the experimental procedure was carried out in a stainless steel radon chamber for 172.52 hours, with a volume of $50L$. A commercial radon source ($RN-1025$, Pylon Electronics, Canada) was used as a radon source in this chamber, as shown in Fig. 2.11. This radon chamber was connected to a radon Mapper monitor to measure the radon concentration, as shown in Fig. 2.12.

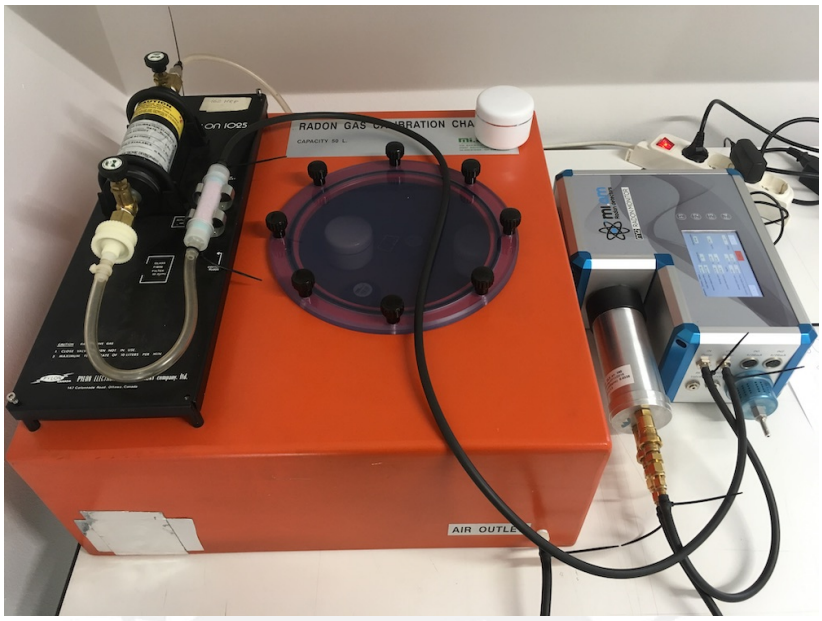

Fig. 2.11 Experimental setup to measure radon in a radon chamber.

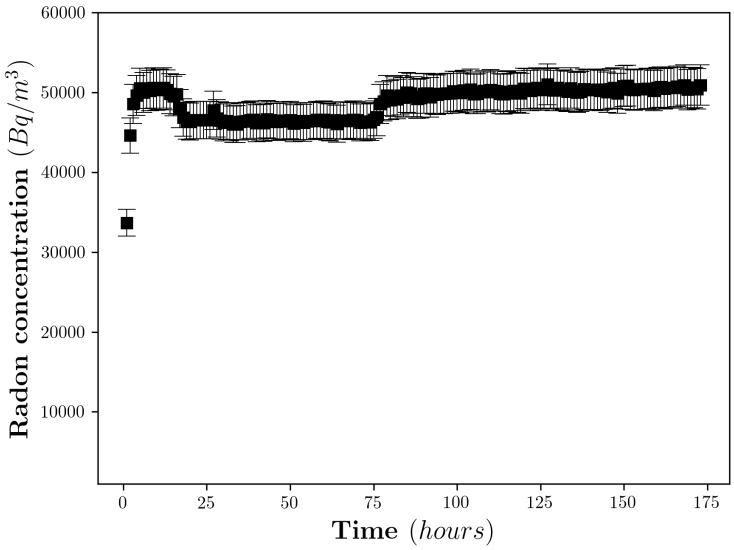

Fig. 2.12 The build up of radon concentration inside the chamber measured with radon Mapper monitor.

Fig. 2.12 depicts that the monitors were exposed to $(9483.1 \pm 118.5) kBqh/m^3$ during 175 hours inside the radon chamber. Ten non-strippable LR-115 (Dosirad, $112\mu m$ thick) detectors inside ten CDC and five CR-39 (*TASTRACK*®, $1mm$ thick) detectors in five commercial *RadOUT*® monitors (designed by MI.AM s.r.l.) were placed in the radon

chamber. After irradiation, LR-115 detectors were chemically etched in $2.5N\ NaOH$ solution at $(60 \pm 0.05)^{\circ}C$ for 90 minutes, and CR-39 detectors were etched in a $6.25N\ NaOH$ solution at $(97.3 \pm 0.05)^{\circ}C$ for 60 minutes. Detectors were rinsed with distilled water for 1 hour and were dried in an absorbent paper for 24 hours. Finally, we counted tracks of these detectors using the *Polytrack*®system (https://miam.it/en/politrack/). This reading system uses a $4x$ objective. The bulk etch rate (V_b) was calculated by a variant of the gravimetric approach suggested by [86], according to the equation:

$$V_b = \frac{96.875\left(1 - \frac{m_f}{m_i}\right)}{t_{etching}} \tag{2.21}$$

where m_f is the mass after etching the detector, m_i is the mass before etching the detector, and $t_{etching}$ is the etching time (90 minutes).

The masses were measured using an analytical balance with a precision of $0.001g$. The V_b is $(3.203 \pm 0.037)\mu m/h$, and it has been used for calculations.

As described above, simulation A is computed using different radon exposures. Each exposure gives some track densities. To include the f_1 fraction dependences, we calculate the total sensitivity using $f_1 = 0$, $f_1 = 0.5$ and $f_1 = 1$. Results are shown in Fig. 2.13, Fig. 2.14, Fig. 2.15 and Fig. 2.16.

Fig. 2.13, Fig. 2.14, Fig. 2.15 and Fig. 2.16 show a linear fit with an intercept equal to zero for the simulated data because the slope-intercept equation form

$$\rho_d = CF \cdot E_{rn} \tag{2.22}$$

where ρ_d is the track density and CF is the total sensitivity or calibration factor, does not have an independent term. In other words, there are no tracks at null radon exposure. In this case, the slope represents the total sensitivity. For each V function, three sensitivities represent the maximum value $(f_1 = 1)$, the intermediate value $(f_1 = 0.5)$ and the minimum value $(f_1 = 0)$. These three results are expressed in the uncertainty limits, where the lower limit represents $f_1 = 0$ and the high limit $f_1 = 1$, as shown in Table. 2.4.

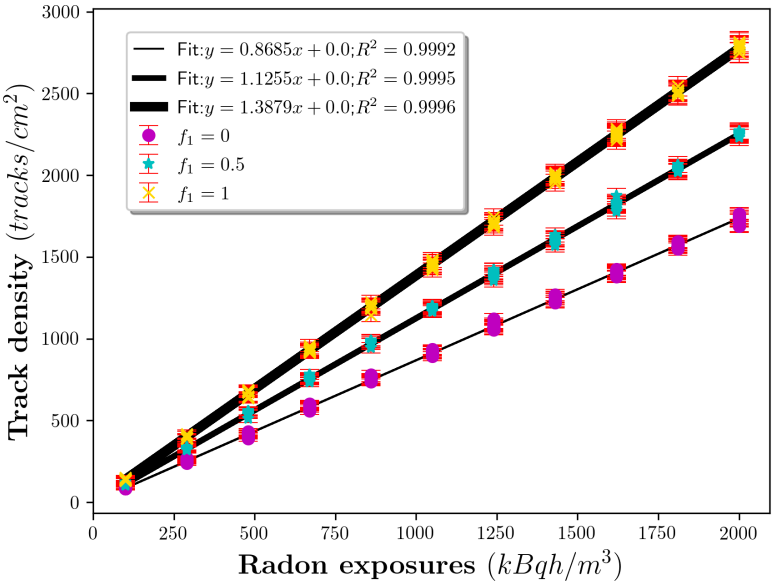

Fig. 2.13 Calibration curves generated by simulation *A* with function *A*. Each slope of the linear curves represent the calibration factor. The standard deviation is represented by the error bars.

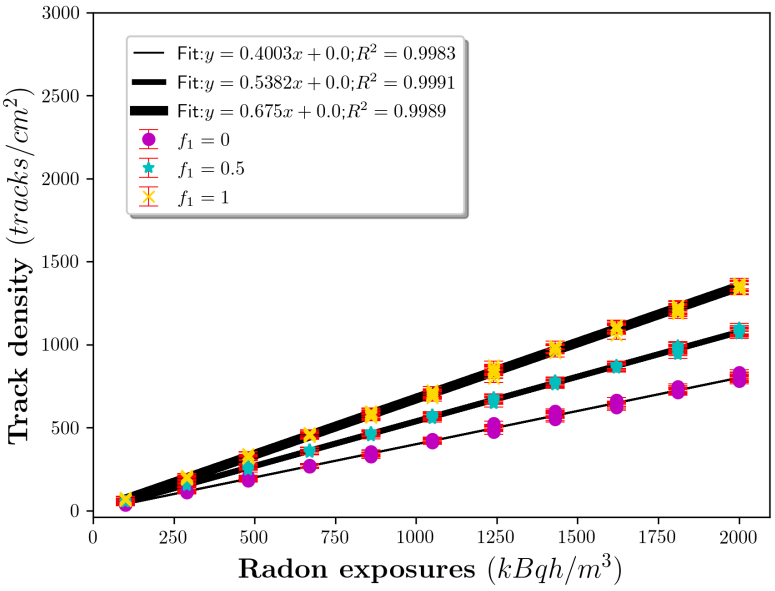

Fig. 2.14 Calibration curves generated by simulation *A* with function *B*.Each slope of the linear curves represent the calibration factor. The standard deviation is represented by the error bars.

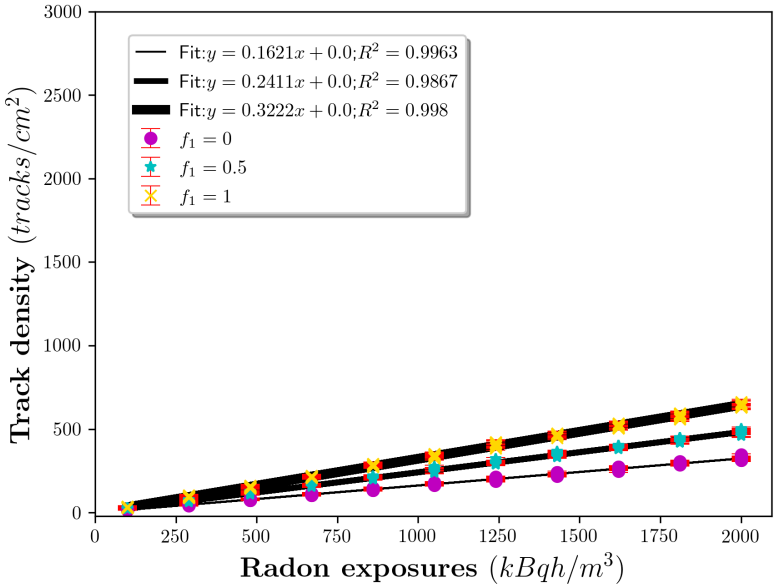

Fig. 2.15 Calibration curves generated by simulation *A* with function *C*.Each slope of the linear curves represent the calibration factor. The standard deviation is represented by the error bars.

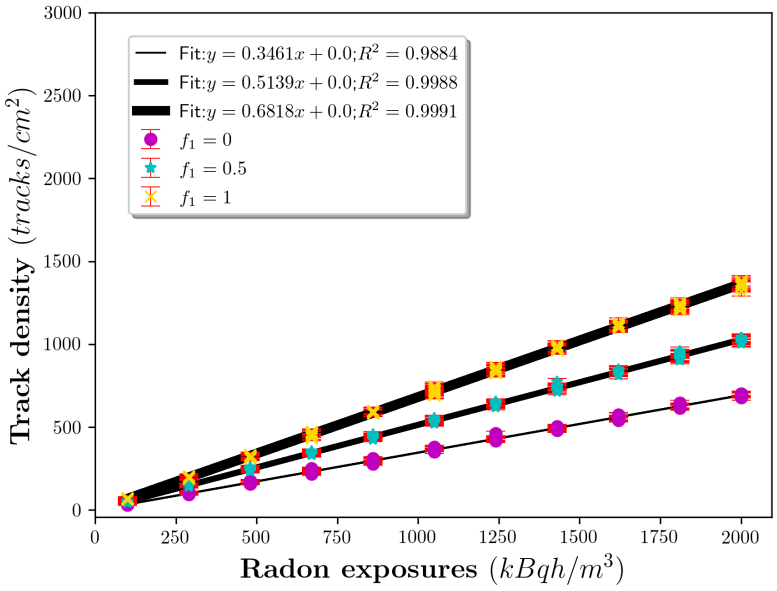

Fig. 2.16 Calibration curves generated by simulation *A* with function *D*.Each slope of the linear curves represent the calibration factor. The standard deviation is represented by the error bars.

Table 2.4 Calibration factors using the simulation A with V functions from Table. 2.3.The error limits are represented by $f_1 = 0$ and $f_1 = 1$, respectively.

V function	Total sensitivity $\left[\frac{tracks/cm^2}{kBq/m^3}\right]$
	Simulation A
A[63]	1.1282 ± 0.2597
B[64]	0.5377 ± 0.1374
C[65]	0.2422 ± 0.0801
D[66]	0.5140 ± 0.1679

Similarly, simulation B is computed by sampling 10^9 stories, and the total sensitivities are expressed based on the f_1 fraction. In other words, upper value was calculated using $f_1 = 1$ and lower value with $f_1 = 0$. Table. 2.5 shows the total sensitivity for each V function.

Table 2.5 Calibration factors using the simulation B with V functions from Table. 2.3.The error limits are represented by $f_1 = 0$ and $f_1 = 1$, respectively.

V function	Total sensitivity $\left[\frac{tracks/cm^2}{kBq/m^3}\right]$
	Simulation B
A[63]	1.1298 ± 0.2941
B[64]	0.5184 ± 0.1658
C[65]	0.2433 ± 0.0781
D[66]	0.5559 ± 0.1766

At this point, experimental results are used to select the best V function. These results give each CDC total track density per unit area, multiplying track densities by each sensitivity, and obtaining the radon exposure that the detectors were exposed to. The radon exposure is shown in Fig. 2.17 and Fig. 2.18 using simulation A and B, respectively.

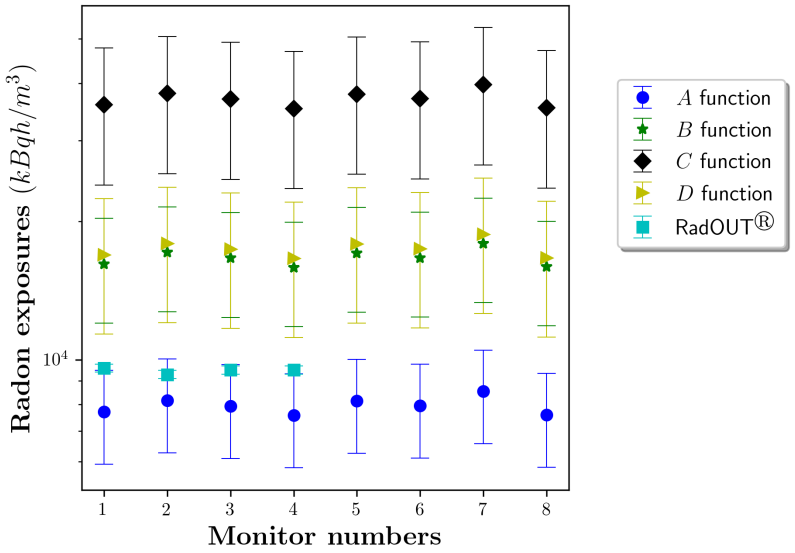

Fig. 2.17 Radon exposures calculated with experimental results and total sensitivities from simulation *A*, using *V* functions from Table. 2.3. Error bars for *RadOUT*® monitor represent the standard deviation.

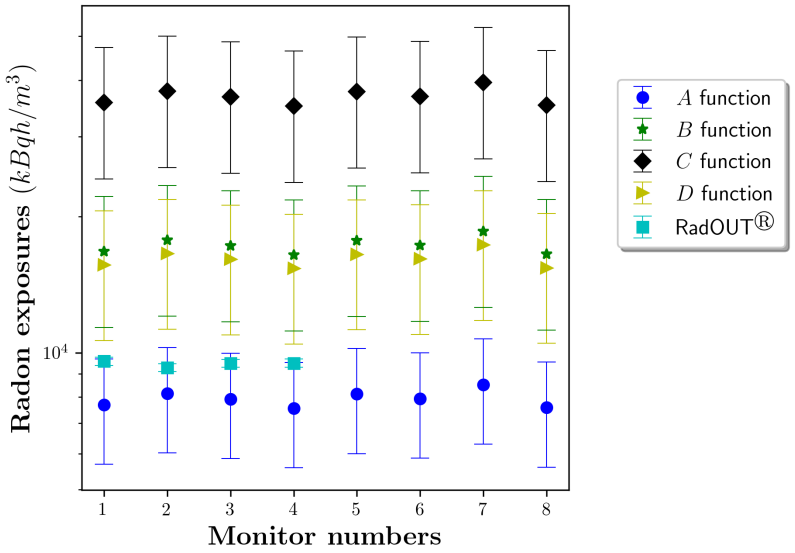

Fig. 2.18 Radon exposures calculated with experimental results and total sensitivities from simulation *B*, using *V* functions from Table. 2.3. Error bars for *RadOUT*® monitor represent the standard deviation.

Fig. 2.17 and Fig. 2.18 show that the *RadOUT*® monitors, as a secondary reference, are within the experimental results when applying the function *A*. We also include the principal reference system (measures using radon Mapper) in Fig. 2.19 and Fig. 2.20 using only the function *A* for both simulations.

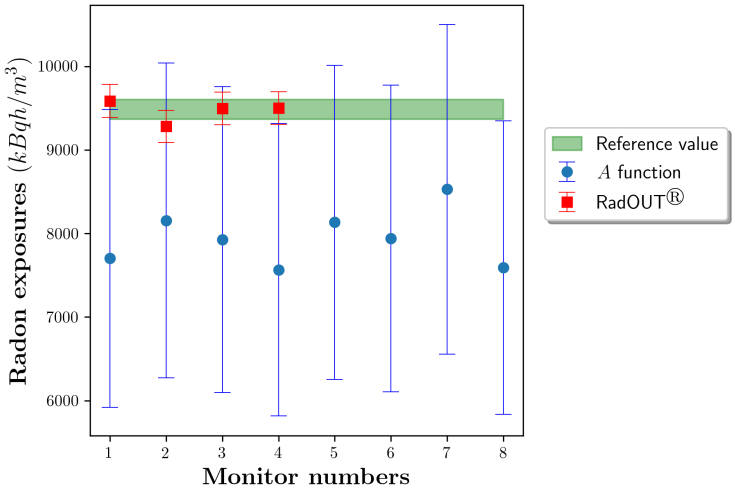

Fig. 2.19 Radon exposures calculated with experimental results and total sensitivities from simulation *A*, using function *A*. Error bars for *RadOUT*® monitor represent the standard deviation.

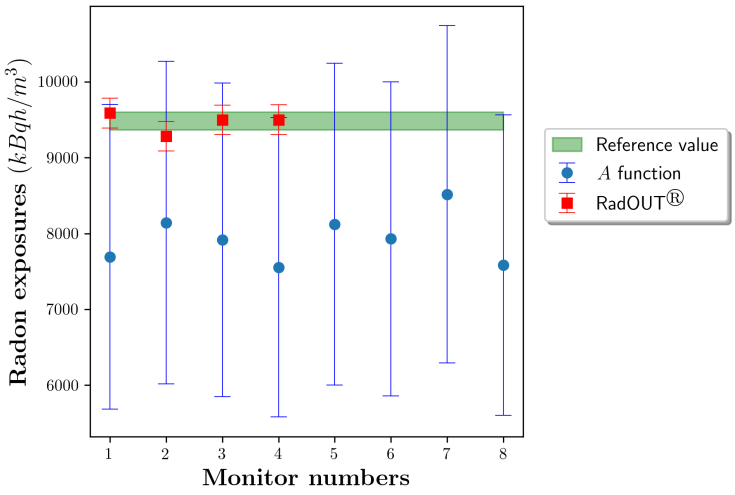

Fig. 2.20 Radon exposures calculated with experimental results and total sensitivities from simulation *B*, using function *A*. Error bars for *RadOUT*® monitor represent the standard deviation.

These figures show that the best V function is the function A. We also observe that the reference value is at the top of a function results, meaning the f_1 value is lower than 0.5. Matching the principal reference (measures using radon Mapper) in Fig. 2.19 and Fig. 2.20, we obtain that simulation A gives $f_1 = 0.2407 \pm 0.0460$ and simulation B gives $f_1 = 0.3579 \pm 0.0449$, slightly similar, including their uncertainties. According to these simulation results, there is no considerable difference for deposited ^{218}Po atoms distribution onto the internal wall when using a conductive or non-conductive chamber. Besides, there is a concordance between both values and those reported by some authors that use conductive chambers, such as [76]. According to [72], it was concluded that the influence of the electric field was not changed significantly the total sensitivity. In other words, there is not considerable difference when comparing a conductive or non-conductive chamber as same as obtained in our simulations.

A mean value equal to 0.9908 ± 0.0290 was obtained concerning the CDC's total sensitivity, considering a mean value $f_1 = 0.2993 \pm 0.0321$.

2.2 LR-115 detector response for very long term exposures

Results from Section (2.1) can be applied when a detector is exposed at short and long term radon exposures inside a CDC. However, when detectors are exposed to very long term radon exposures, results may vary. These different radon exposure levels can be found when measuring radon in sub-soil, indoor and water [87–92]. The radon concentration can vary from 0.1 to $253 kBq/m^3 s$, especially in sub-soil radon measurements [93–98]. Since radon gas exhalation from soils can increase indoor radon concentrations, these too high levels can impact the radiological risk associated with inhaling indoor radon [99, 100]. Concerning neutron physics, very high radon concentrations can increase the thermal neutron background since these high levels produce neutrons by (n, α) reactions [101].

In such a case where radon concentrations are at very high levels, a problem so-called overlapping effect can strongly affect the response of the LR-115 [102–104] when measuring radon concentrations during an extended period. This effect can affect the detector's response because very high radon concentration levels mean a large number of registered alpha particles. These alpha particles are registered as latent tracks formed in the active layer of the detector. After the etching process, a large number of visible tracks are formed, and a visible track has a high probability of being registered in a position where other tracks was placed. Fig. 2.21 shows the overlapping effect in an LR-115 detector.

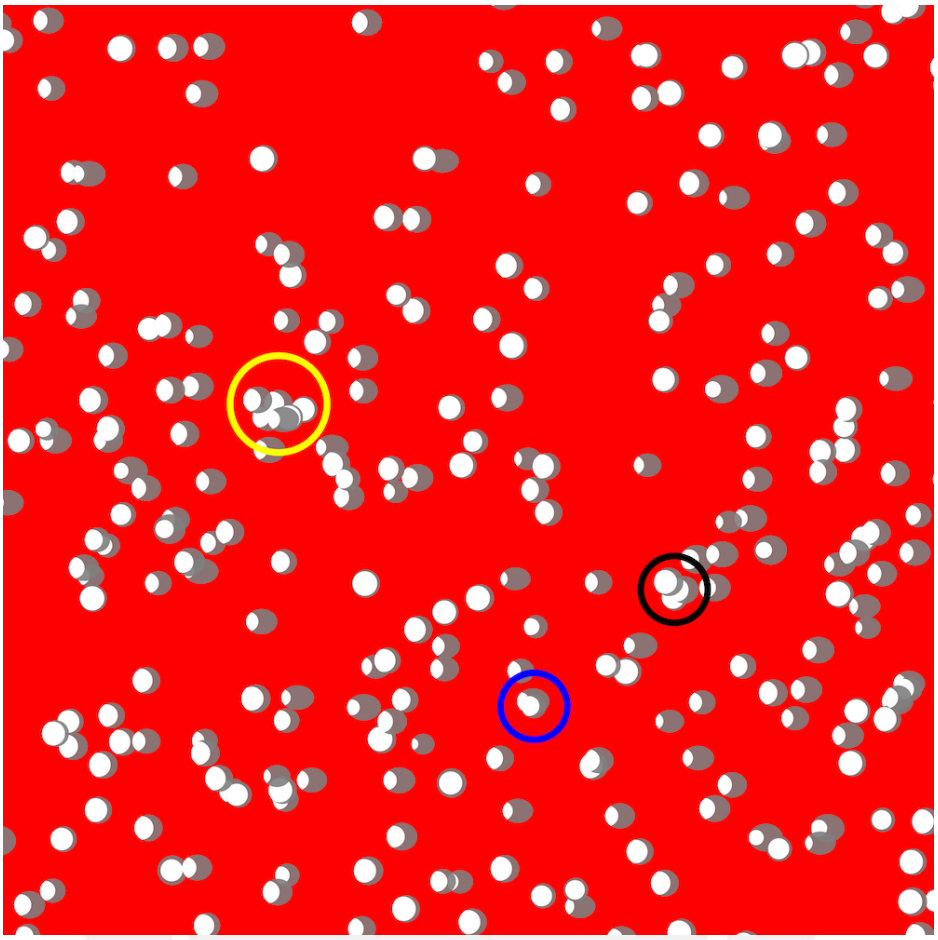

Fig. 2.21 Example of overlapped tracks, as shown in circled colors.

To study and correct the overlapping effect, we use the methodology of simulation A because this simulation samples the number of alpha particles emitted by radon inside the CDC in terms of radon exposure. In the previous chapter, we were able to validate the simulations with the experiment carried out. So we can change some input parameters when applying the methodology in this chapter.

In this chapter, we use an LR-115 detector inside a CDC and the function B from Table. 2.3, since it best describes when detectors are etched in a $2.5N\ NaOH$ solution at $(60 \pm 0.05)^{\circ}C$ for 2 hours. An LR-115 detector inside a CDC is theoretically exposed to $23.15 kBq/m^3$ of radon concentration during three months, or similarly, to $50000 kBqh/m^3$ radon exposure. According to the methodology, we sample $V_{CDC} \cdot 50000 \cdot 3.6$ uniform random positions where alpha particles are emitted by radon decay. For radon progeny, we take into account the f_1 fraction calculated in the previous chapter. In other words, we sample $V_{CDC} \cdot 50000 \cdot 3.6 \cdot f_1$ uniform random positions for ^{218}Po in air state, $V_{CDC} \cdot 50000 \cdot 3.6 \cdot (1 - f_1)$ for ^{218}Po in deposited state and $V_{CDC} \cdot 50000 \cdot 3.6$ for ^{214}Po in the full deposited state. These

positions are sampled in cylindrical coordinates, as in Sub-section (2.1.4). Their directions are sampled using spherical coordinates as follows:

$$\begin{aligned} Cos(\theta_4) &= -2\pi\xi_{11} + 1 \\ \phi &= 2\pi\xi_{12} \end{aligned} \tag{2.23}$$

where ξ_{11} and ξ_{12} are random uniform numbers between 0 and 1. As Appendix A, the algorithm select alpha particles from radon and its progeny that reach the detector surface and generate visible tracks. Using geometrical and graphical libraries in Python, visible tracks can be graphically illustrated as shown in Fig. 2.22, Fig. 2.23 and Fig. 2.24.

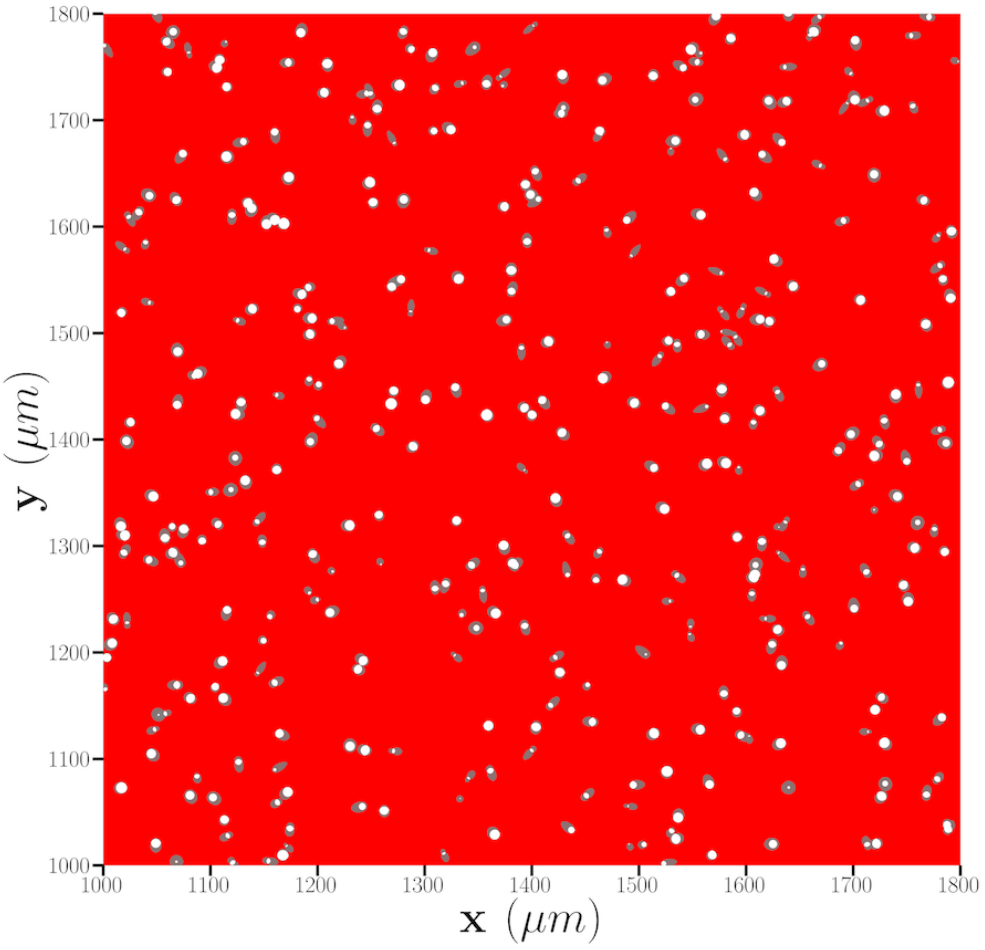

Fig. 2.22 Simulated visible tracks in a $(0.08x0.08)cm^2$ field of vision $(0.10cm < x < 0.18cm$ and $0.10cm < y < 0.18cm)$ for an exposure of $E = 50000kBqh/m^3$.

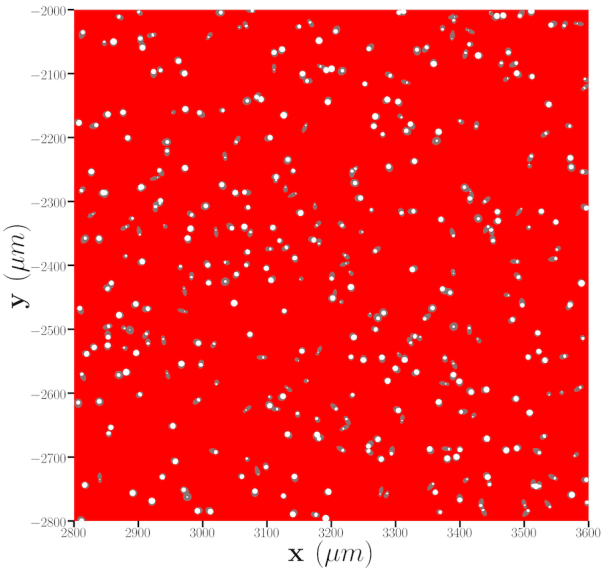

Fig. 2.23 Simulated visible tracks in a $(0.08x0.08)cm^2$ field of vision $(0.28cm < x < 0.36cm$ and $-0.28cm < y < -0.20cm)$ for an exposure of $E = 50000kBqh/m^3$.

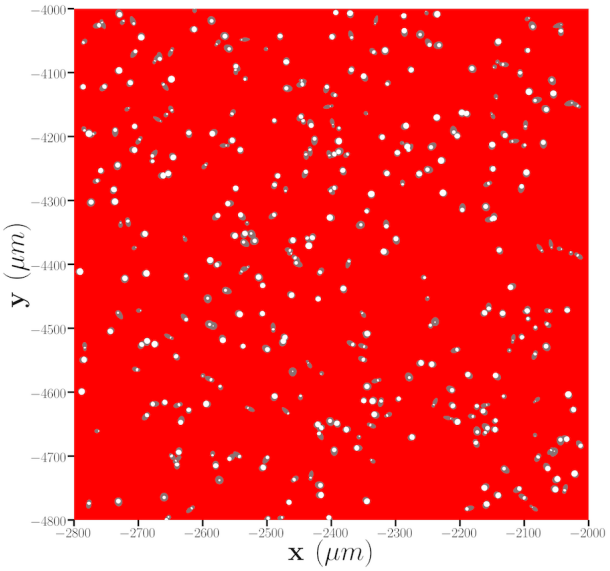

Fig. 2.24 Simulated visible tracks in a $(0.08x0.08)cm^2$ field of vision $(-0.28cm < x < -0.20cm$ and $-0.48cm < y < -0.40cm)$ for an exposure of $E = 50000kBqh/m^3$.

Fig. 2.22, Fig. 2.23 and Fig. 2.24 show different fields of vision of $0.08x0.08cm^2$ for a LR-115 detector inside the CDC exposed to $50000kBqh/m^3$. It is easy to observe the presence of the overlapping effect. More than three ones even overlap some visible tracks. Fig. 2.22, Fig. 2.23 and Fig. 2.24 can be processed by an image processing, such as ImageJ, to count the non-overlapped tracks, since Fig. 2.22, Fig. 2.23 and Fig. 2.24 are digital images where there is no external noise, as shades or mechanical defects that make it easy to read. However, several process image algorithms need to remove the microscope's real detector images or reduce the noise.

According to [103], the number of non-overlapped tracks (N_{n-ov}) and radon exposure are related by the following equation:

$$N_{n-ov}(E) = E_{rn} \cdot CF \cdot A_d \cdot exp(-F \cdot A_t \cdot E_{rn} \cdot CF) \tag{2.24}$$

where F is a conversion factor, A_d is the area of the field of view and A_t is the mean value of the areas of the visible tracks. So we must compare this equation with simulations to obtain the best F value. Fig. 2.25 and Fig. 2.26 shows simulation results fitted by Eq. (2.24).

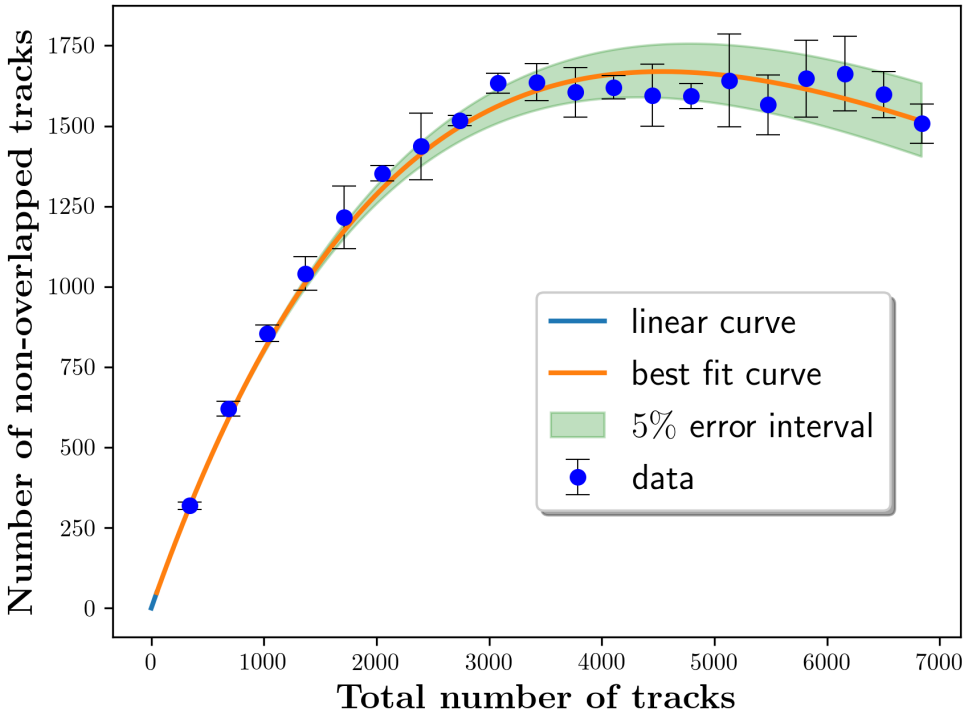

Fig. 2.25 The relation between non-overlapped and total number of tracks in a field of view of $(0.08x0.08)cm^2$ per radon exposure. Error bars represent the standard deviation.

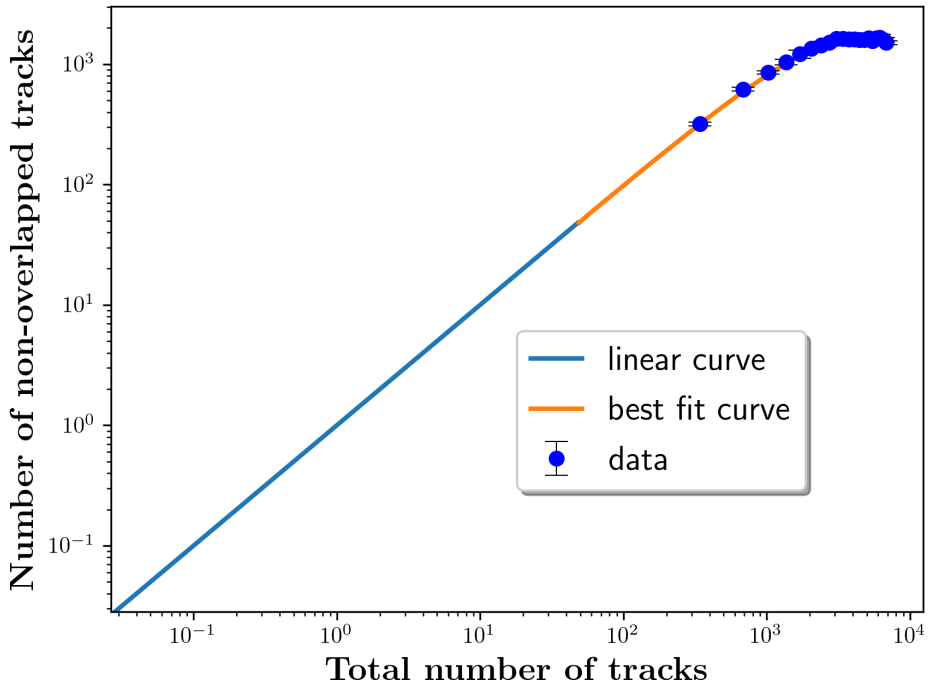

Fig. 2.26 Log-scale plot of Fig. 2.25.

Simulation results are within the model with F equal to $1.6491 \pm 5\%$. This obtained F value is applicable for radon measurements with an LR-115 detector exposed inside a CDC and using the etching conditions as mentioned earlier. Besides, as seen in Fig. 2.26, the minimum exposure limit at which the overlapping correction can be applied is when the total number of tracks equals the number of non-overlapped tracks. The minimum value is approximately $7049 kBqh/m^3$. Lower values than the minimum do not have the overlapping effect. In Fig. 2.26, the liner curve represents no overlapping effect and the overlapping correction must be only applied for values greater than $7049 kBqh/m^3$.

Chapter 3

LR-115 detector exposed in unconventional bare mode

3.1 Detectors exposed to natural radiation

3.1.1 General remarks

In radon measurements, the active layer ($10\mu m$ of cellulose nitrate) of the LR-115 usually registers alpha particles emitted by radon and its progeny decays. However, the non-active layer ($100\mu m$ of polyester) of the LR-115 does not register alpha particles, it only acts as a support for nitrocellulose (active-layer). In order to study the response of the detector's non-active layer, we explain the procedure of exposing LR-115 detectors by their non-active layer in free contact with natural radiation. At this point, we collect some information about electromagnetic radiations that can affect the LR-115 detector. For instance, the manufacturer also remarks that LR-115 detectors are insensitive to electrons, gamma rays, X-rays or infra-red radiation. These radiations, on the other hand, can alter the molecular structures and properties of polymers (both layers) [105, 106, 44, 107–109]. In exposures to natural environment, UV radiation is almost inevitable, and this radiation is divided into three bands (UV-A, UV-B and UV-C). According to [110], a high percentage of UV-A $(320-400)nm$ reach the Earth's surface, while for the UV-B $(280-320)nm$ is a low percentage. Besides, some authors [111–115] have been studied that the high UV radiation can also alter the mechanical properties of the active and non-active layer by scission reaction. This reaction breaks the boundaries and contributes to deformation and discolouration of LR-115.

3.1.2 Experimental methodology in situ

In this section, several LR-115 detectors were exposed with the non-active layer facing the outdoor air. As mentioned above, there is a large amount of UV radiation in outdoor environment, so that this type of radiation may irradiate the non-active layer. Several experiments were carried out taking into account indispensable conditions (seasons, places, altitudes, locations, arrangements, irradiation time and etching time) to study the possible cause-effect relationship which may have some radiation and the non-active layer.

First, we chose three different seasons: summer (S_S), winter (S_W), and autumn (S_A). For each season, we choose three municipal districts in the Metropolitan area of Lima (D_{SM}, D_M, D_C) with about 30 kilometres apart from each other. For each municipal district, we chose three altitudes of 0 (A_0), 4.5 $(A_{4.5})$ and 9.5 $(A_{9.5})$ meters from ground level. For each altitude, detectors were placed on outdoor (P_O) and indoor (P_I) places. For each place, detectors were placed on twelve configurations, as shown in Fig. 3.1.

The active layer is represented by the red rectangle in Fig. 3.1, while the blank rectangle represents the non-active layer. There are two LR-115 detectors in configurations 8, 9, 10, and 11, as LR-115-A, in close contact with the support and the LR-115-B with the air. In the experiments, we used two thicknesses of $PP2500$ transparency film, 0.14 and $0.84mm$, in configurations 3,4,5 and 6. In configuration 7, the UV filter thickness is $0.8mm$; and in configuration 12, the lead sheet is $4.50mm$ thick. Detectors were exposed during 10 (I_10), 20 (I_20) and 30 (I_30) days. After the exposition, detectors were chemically etched in $2.5N$ $NaOH$ solution at $60°C$ for 30 (E_{30}), 60 (E_{60}) and 90 (E_{90}) minutes for each exposition time. Finally, each detector was observer under an optical microscope (Leica - DM LM). Fig. 3.2 shows a map of the entire experiment described above.

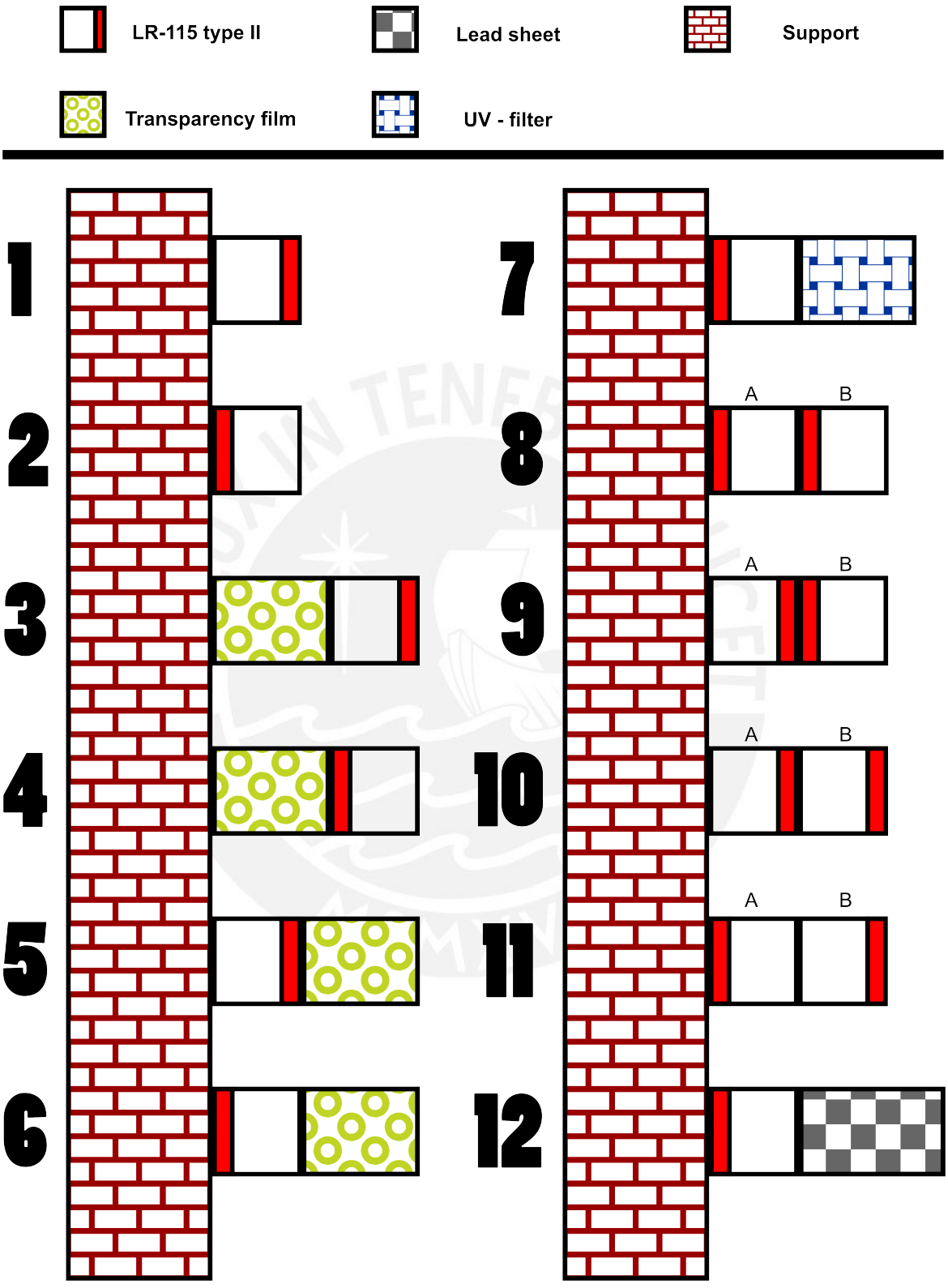

Fig. 3.1 Twelve LR-115 configurations used in the experimental procedure.

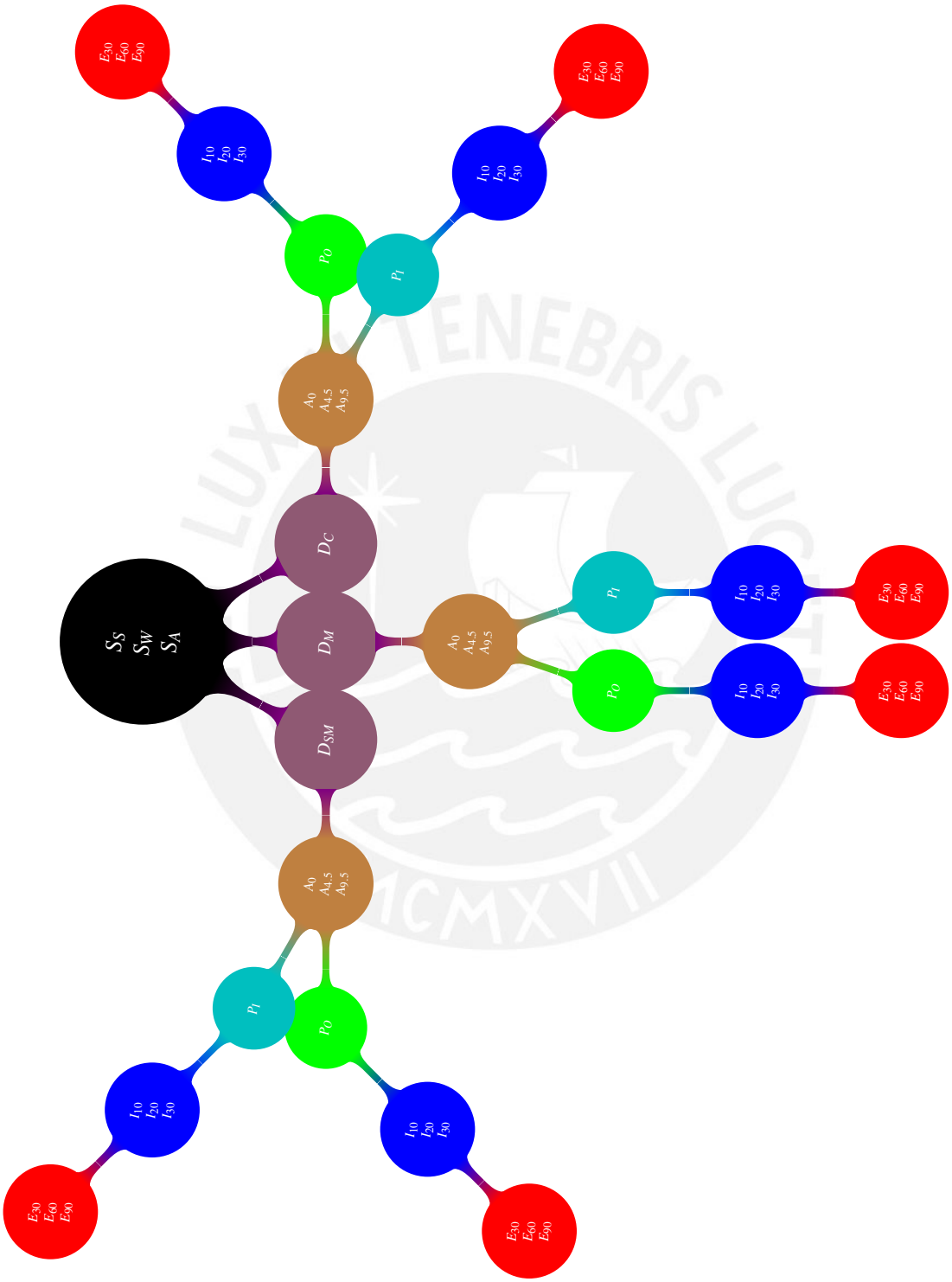

Fig. 3.2 Map of the conducted experiment, using codes from Section (3.1.2).

After experimenting, it is observed that some detectors do not register anything at all. However, others record different tracks in the form of concentric rings tracks (CRTs), similar to interference patterns, as shown in Fig. 3.3, Fig. 3.4, Fig. 3.5 and Fig. 3.6.

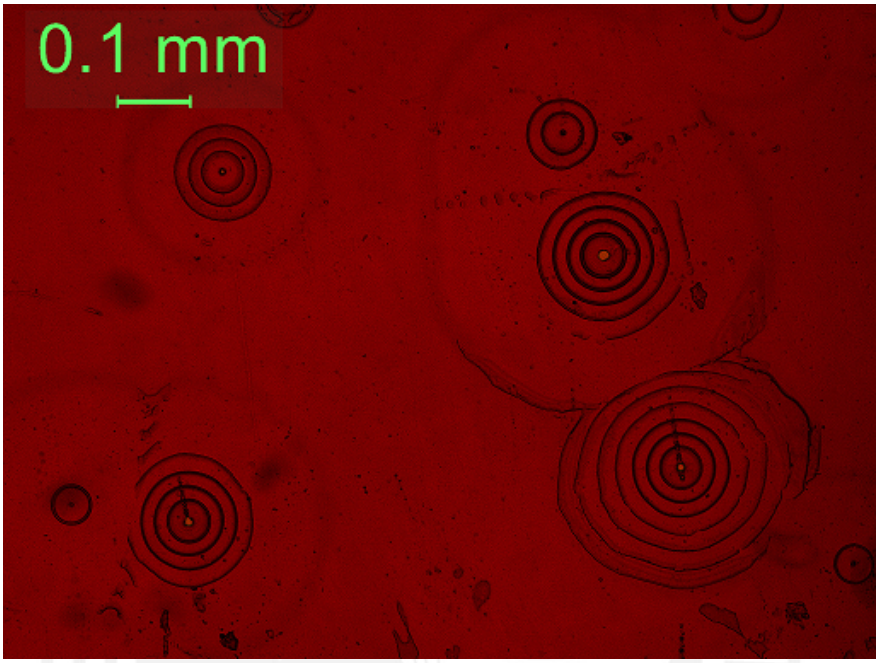

Fig. 3.3 Optical microscopic images of CRTs formation (1).

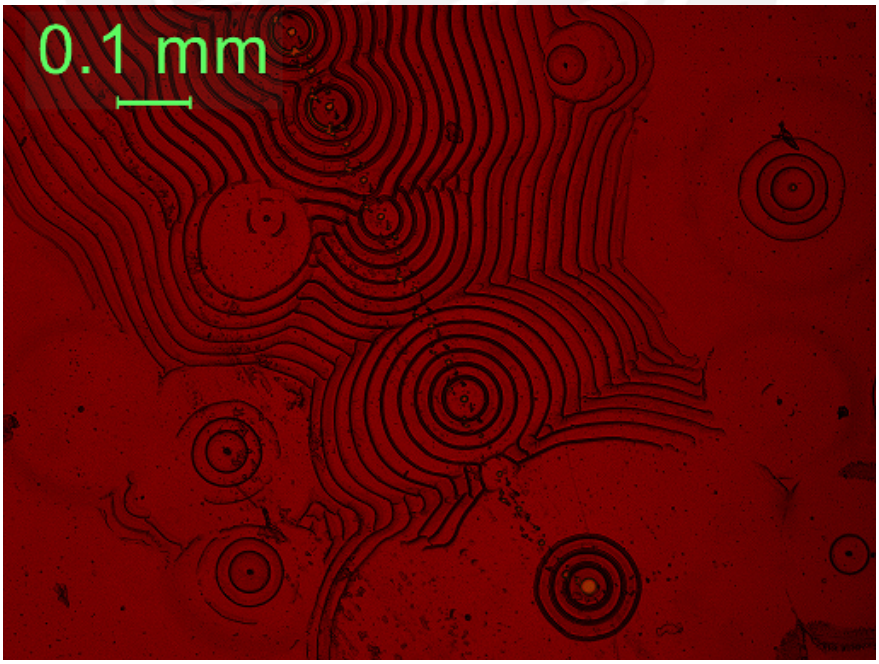

Fig. 3.4 Optical microscopic images of CRTs formation (2).

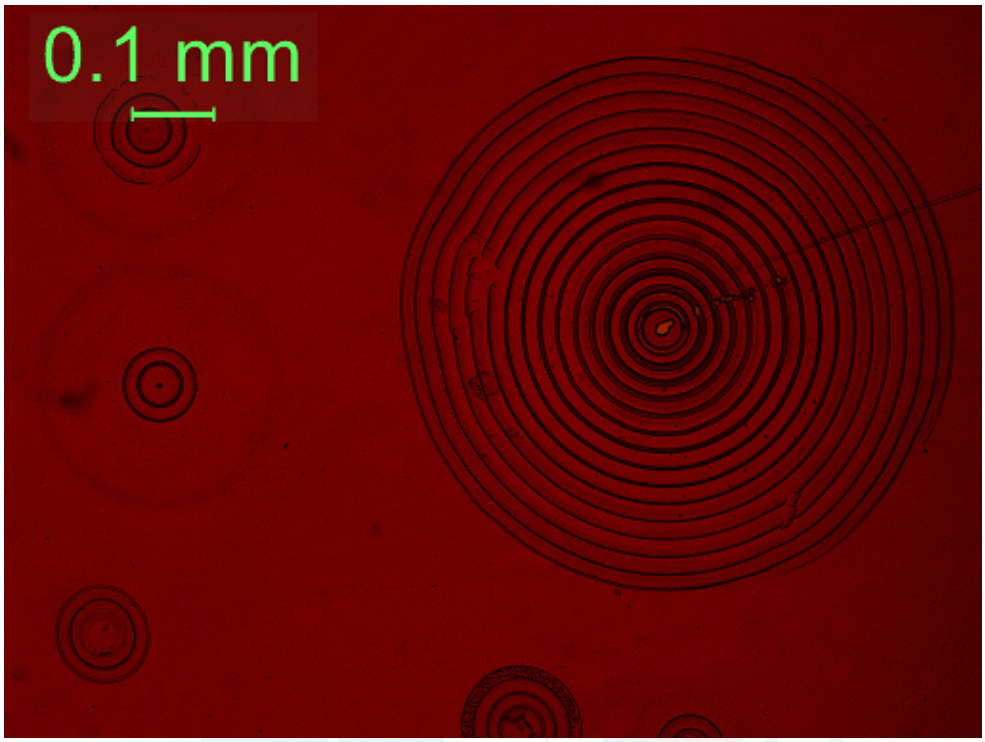

Fig. 3.5 Optical microscopic images of CRTs formation (3).

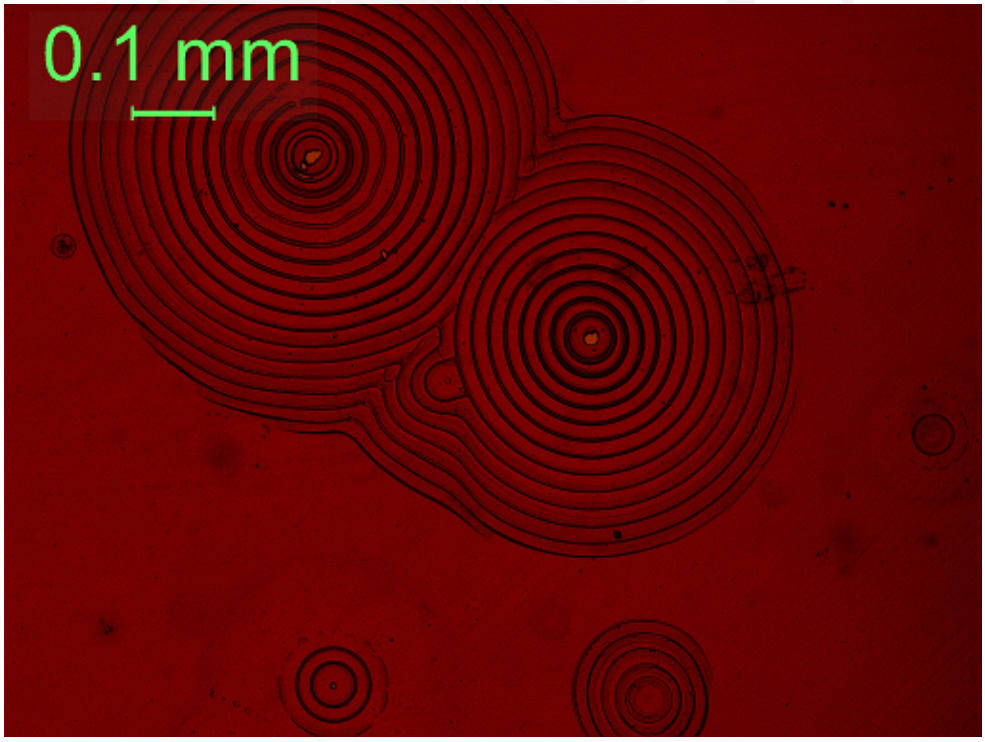

Fig. 3.6 Optical microscopic images of CRTs formation (4).

Table. 3.1 shows the results for all possible combinations of the conditions aforementioned. In this table, the checkmark represents CRTs formation on the active layer while no CRTs formation are marked using a cross mark.

Table 3.1 Results obtained in the twelve configurations for all possible combinations of seasons of the year (S_S, S_W, S_A), places in Metropolitan Lima (D_{SM}, D_M, D_C), and heights above ground level $(A_0, A_{4.5}, A_{9.5})$.

	P_O									P_I								
Codes	I_{10}			I_{20}			I_{30}			I_{10}			I_{20}			I_{30}		
	E_{30}	E_{60}	E_{90}	E_{30}	E_{60}	E_{90}	E_{30}	E_{60}	E_{90}	E_{30}	E_{60}	E_{90}	E_{30}	E_{60}	E_{90}	E_{30}	E_{60}	E_{90}
1	×	×	×	×	×	×	×	×	×	×	×	×	×	×	×	×	×	×
2	×	×	×	✓	×	×	✓	×	×	×	×	×	×	×	×	×	×	×
3	×	×	×	×	×	×	×	×	×	×	×	×	×	×	×	×	×	×
4	×	×	×	✓×	×	×	✓×	×	×	×	×	×	×	×	×	×	×	×
5	×	×	×	×	×	×	×	×	×	×	×	×	×	×	×	×	×	×
6	×	×	×	✓×	×	×	✓×	×	×	×	×	×	×	×	×	×	×	×
7	×	×	×	×	×	×	×	×	×	×	×	×	×	×	×	×	×	×
8	×	×	×	×✓	×	×	×✓	×	×	×	×	×	×	×	×	×	×	×
9	×	×	×	×✓	×	×	×✓	×	×	×	×	×	×	×	×	×	×	×
10	×	×	×	×	×	×	×	×	×	×	×	×	×	×	×	×	×	×
11	×	×	×	×	×	×	×	×	×	×	×	×	×	×	×	×	×	×
12	×	×	×	×	×	×	×	×	×	×	×	×	×	×	×	×	×	×

According to Table. 3.1, CRTs are not formed when detectors were placed in indoor places. Detectors irradiated fo 20 or 30 minutes in outdoor places and etched for 30 minutes in configuration 2, 4, 6, 8, or 9 formed CRTs. The checkmark in configurations 4 and 6 reflects CRTs formation in the LR-115 using a $0.14mm$ transparency film, while the cross mark represents a $0.84mm$ transparency film. On the other hand, the checkmarks from configuration 8 and 9 indicate that CRTs are formed on LR-115-B, while the cross marks imply no CRTs formation. In configuration 6, CRTs are formed when using transparency films less than $0.14mm$.

3.1.3 Experimental methodology in laboratory

In this section, an experimental validation of CRTs results was carried out using two certified lasers. A $30mW$ cw He-Ne laser $(632.8nm)$ and a beta barium borate (BBO) crystal pumped by a $3.7mW$ cw diode laser $(400nm)$ were used to irradiate some detectors in a dark room with ambient temperature. Detectors were irradiated for 1, 2, 5, 10 and 20 minutes for each laser. Then they were chemically etched in $2.5N$ $NaOH$ solution at $60^{\circ}C$ for 30 minutes. Finally, we also observed them under the same optical microscope. Results show that the CRTs are only formed by using the BBO laser for 10 minutes, as shown in Fig. 3.7.

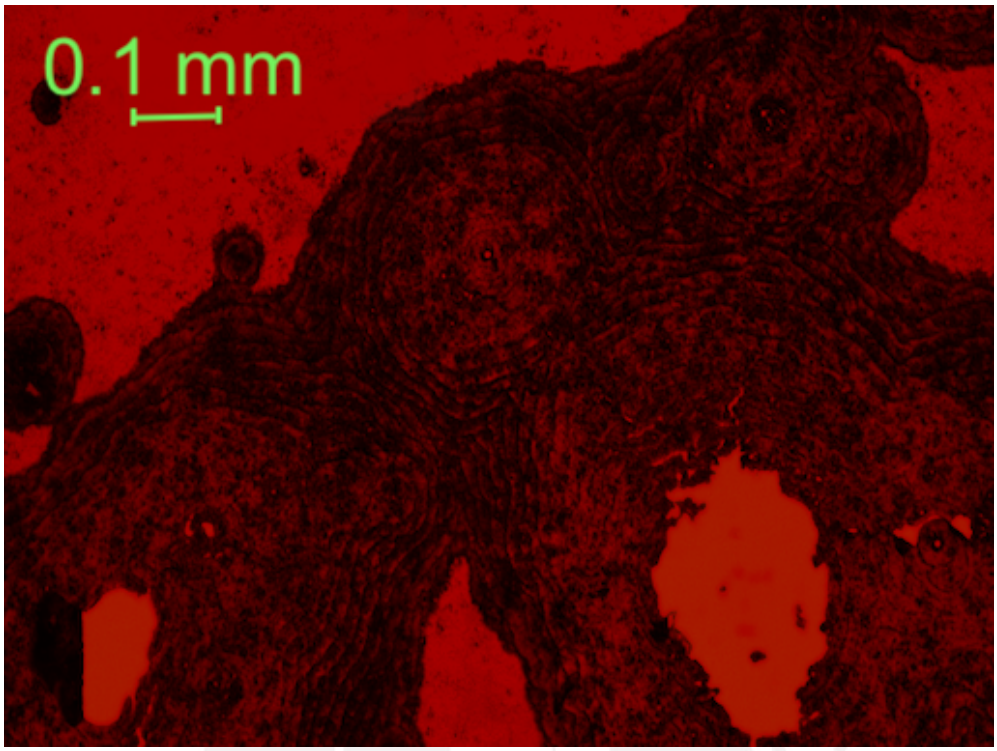

Fig. 3.7 LR-115 detector irradiated during 10 minutes with the BBO laser.

3.1.4 CRTs formation on an LR-115 detector

At $time = 0s$, LR-115 detectors placed in configuration 2,4,6,8 or 9 begin to irradiate with the outdoor agent, as shown in Fig. 3.8.

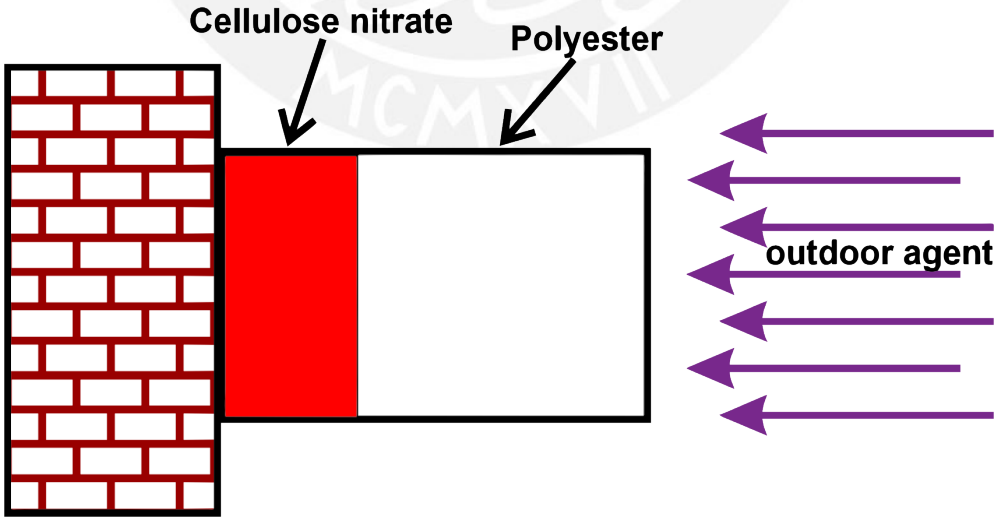

Fig. 3.8 LR-115 irradiated at $time = 0$

A localised point of the non-active layer will then absorb some of the outdoor agent radiation, heating this point [111]. This heating process can alter the molecular structure of the non-active layer producing refractive index changes in this point [116–118]. These changes work as a circular aperture where the remaining radiation can drift through this aperture, producing interference rings in both layers interface [119, 120], as shown in Fig. 3.9.

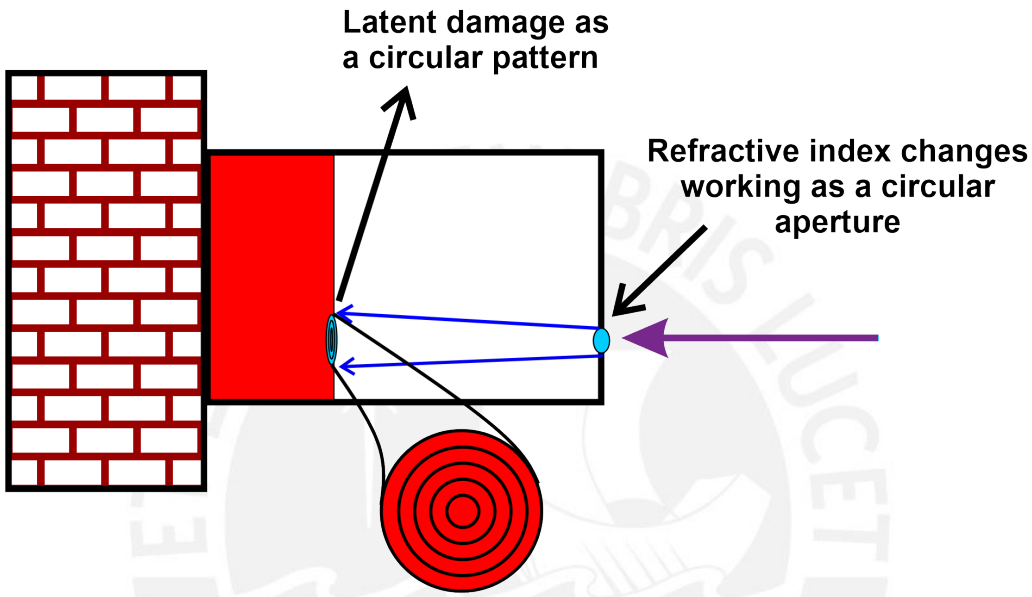

Fig. 3.9 Circular pattern damage formation in layers interface.

During 20 or 30 days of irradiation, it happens that this latent damage in the form of interference rings penetrates the active layer, proportional to the outdoor agent radiation's intensity according to the Airy disk phenomenon. The BBO laser (λ_{BBO}) wavelength is 400nm, and the angular resolution (θ_{res}) is the *arctan* of the non-active layer thickness divided by the distance between the centre of the CRTs and the CRTs first constructive ring. So the diameter D_a of the 'aperture' (Airy disk radius) can be calculated by using the Rayleigh criterion [121]:

$$D_a = \frac{1.22 \cdot \lambda_i}{sin(\theta_{res})} \tag{3.1}$$

If the calculation is made in Eq. (3.1), the diameter of the 'aperture' is equal to $(1467.68 \pm 183.17)nm$. Due to this 'aperture', a cylindrical profile is formed in the active layer, as shown in Fig. 3.10.

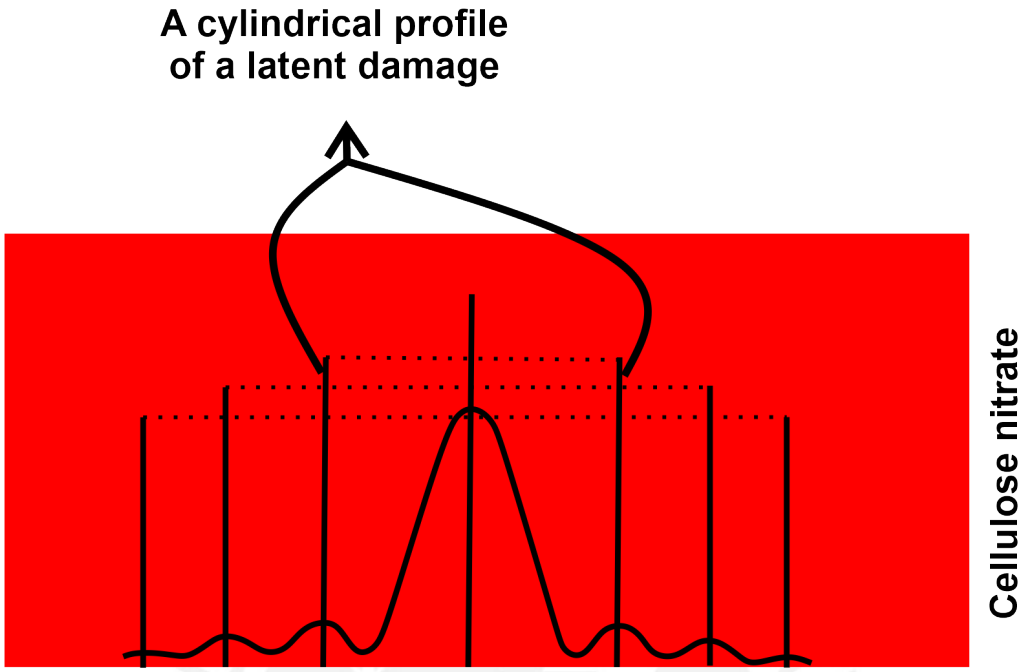

Fig. 3.10 Cylindrical profile formation in the active-layer after 20 days of irradiation.

After etching detectors for 30 minutes, the chemical solution penetrates the latent damage in the cylinder profile's geometrical form. In this process, the etching progresses along the detector's undamaged region with the rate Vt (track etch rate), and then it goes along the cylinder profile with the rate $V_b = 3.28um/h$ (bulk etch rate). Finally, the CRT is formed, as shown in Fig. 3.11.

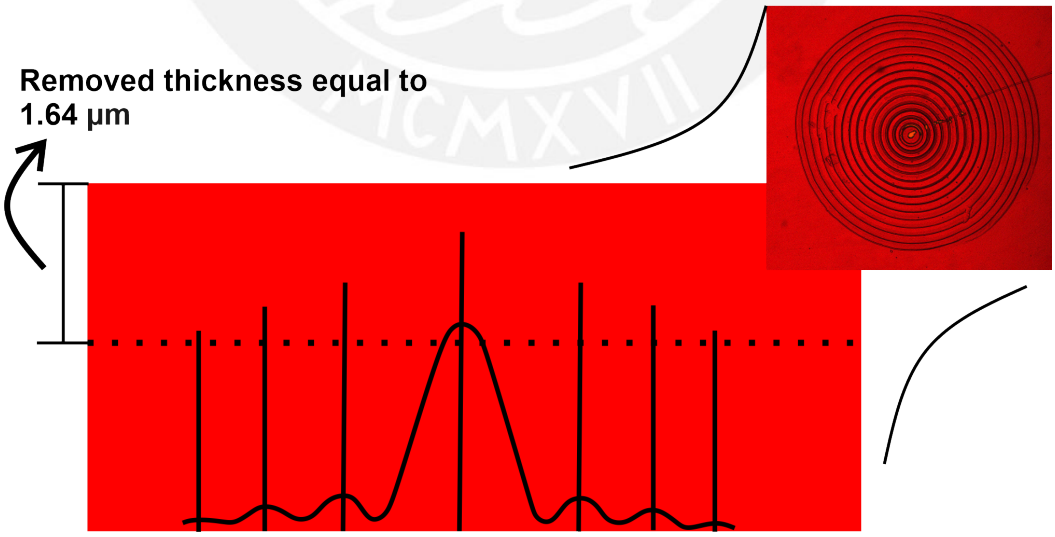

Fig. 3.11 CRTs formation after etching process.

3.1.5 The outdoor agent radiation

At this point, we can use results from Section (3.1.2) to estimate the wavelength of the outdoor agent radiation by using Eq. (3.1), the approximately 'aperture' value and the different angular resolutions from Fig. 3.3, Fig. 3.4, Fig. 3.5 and Fig. 3.6. In Fig. 3.12, we obtain the wavelength distribution of the outdoor agent radiation.

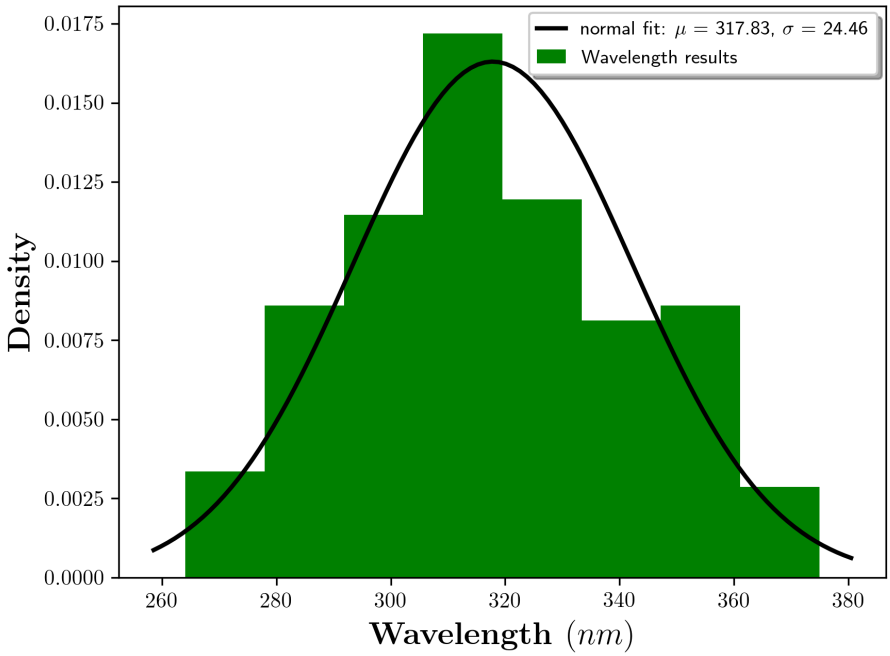

Fig. 3.12 The wavelength distribution of outdoor agent that produce CRTs

Fig. 3.12 shows that the most probable value is $317.83 \pm 24.46nm$. It may mean that the outdoor agent is the UV radiation, either UV-A or UV-B.

3.2 Detectors exposed at the neutron source

As we said previously, some solid-state nuclear track detectors are insensitive to beta particles, x-rays and gammas. However, neutrons are neutral particles and do not directly produce ionisations and excitations in the detector. Their registration is given by recoil nuclei $(C, H, O, {}^{7}Li)$ and particles generated in nuclear reaction during their interaction process, such as ${}^{10}B(n,\alpha){}^{7}Li$, ${}^{6}Li(n,\alpha){}^{3}H$ [122]. In this case, we use detectors coupled with converters to generate a high rate of (n,α) reactions. These converters could be ${}^{6}Li$ or ${}^{10}B$, which mainly interacts with thermal neutrons $(E < 0.5eV)$. For instance, the converter ${}^{6}Li$ has an effective

cross-section of 940*barns* and creates alpha particles with kinetic energies of 2.5*MeV* in a (n,α) reaction. On the other hand, ^{10}B has an effective cross-section of 3840*barns* and alpha particles with two different energies of $1.47MeV(94\%)$ and $1.78MeV(6\%)$. Here, we want to estimate a detector's efficiency coupled with a converter because this arrangement is usually used in neutron dosimetry. An isotopic neutron source must irradiate the arrangement to simulate this process and estimate the efficiency, as shown in Fig. 3.13.

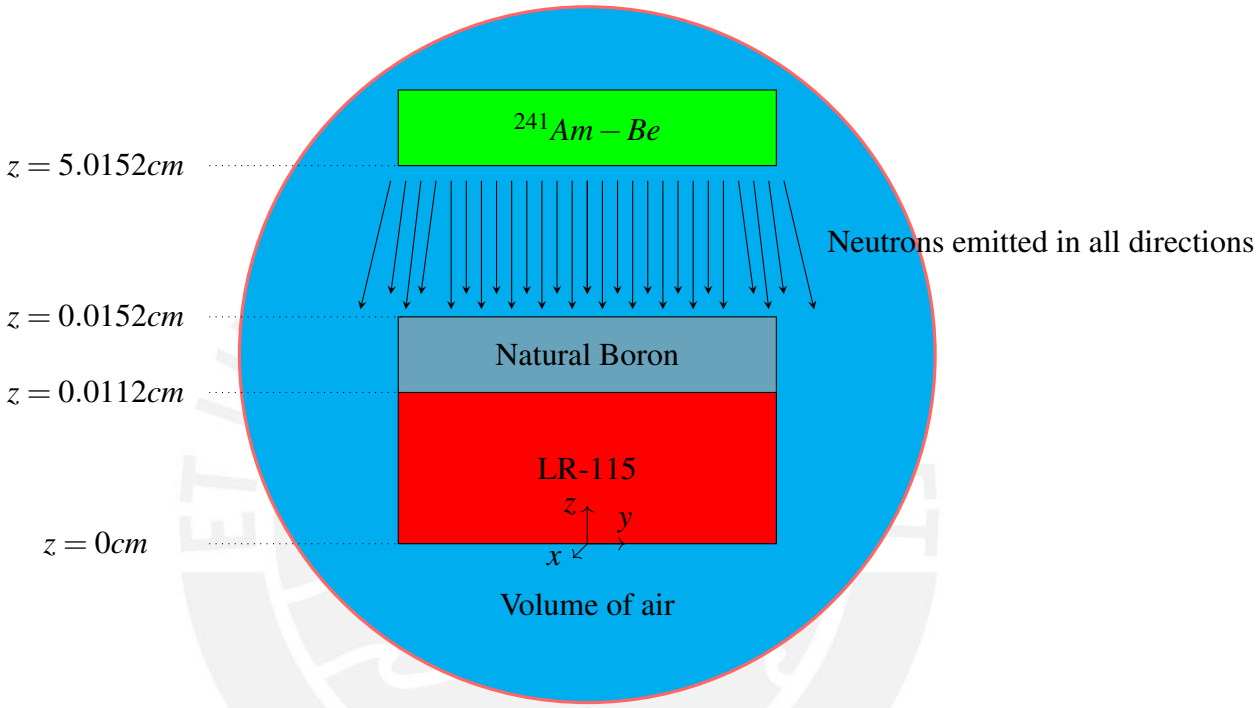

Fig. 3.13 Converter-detector arrangement irradiated by an $^{241}Am-Be$ neutron source.

Fig. 3.13 shows a $^{241}Am-Be$ source with an activity of 20*Ci*, an LR-115 detector and a natural boron converter of 0.004*cm*.

3.2.1 Alpha particle distribution in the converter film

We can assume that alpha particles in the converter film follow a uniform distribution. However, we can determine a given distribution by using external codes such as *MCNP*6.1.0.

To estimate the distribution of the alpha particles in the converter film, we divided the converter into 250 known sub-volumes (cells), as shown in Fig. 3.14.

In each cell, the number of Q reactions $(reactions/cm^3 s)$ was calculated as follows:

$$Q = C\int_{10^{-9}}^{20} \phi_n(E_n)\cdot\sigma(E_n)\cdot dE_n \tag{3.2}$$

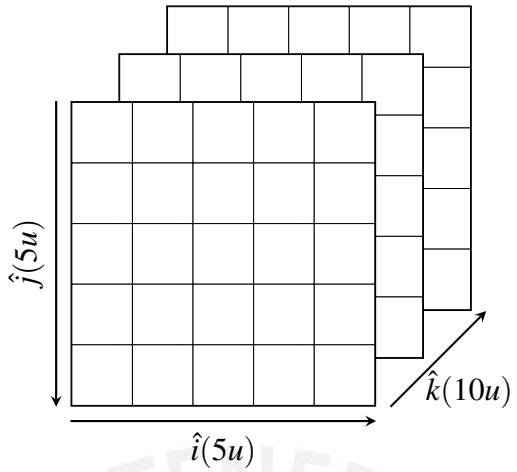

Fig. 3.14 Converter divided into 250 cells.

where ϕ_n is the neutron flux, σ is the cross-section, C is the normalisation constant, and E_n is the neutron's energy. This constant represents the number of atoms distributed in the volume of the converter in term of barns. For the converter, C constant is equal to $0.026\frac{atoms}{barns \cdot cm}$.

In the *MCNP*6.1.0 code, we use the dimension, the material, and the converter's density and the detector. The neutron source has an activity of $20Ci$, which means $740x10^9$ alpha particles per second. According to [123], this source has a neutron production of $82 \pm 9.8\%n/s$ per 10^6 emitted alpha particles. So the neutron emission rate is equal to $60.68 \times 10^6 s^{-1}$. We also use the $FM4$ card to determine the number of the (n,α) reactions in each cell. Fig. 3.15, Fig. 3.16, Fig. 3.17, Fig. 3.18, Fig. 3.19, Fig. 3.20, Fig. 3.21, Fig. 3.22, Fig. 3.23 and Fig. 3.24 show the spatial distribution of the number of (n,α) reactions produced in the natural boron.

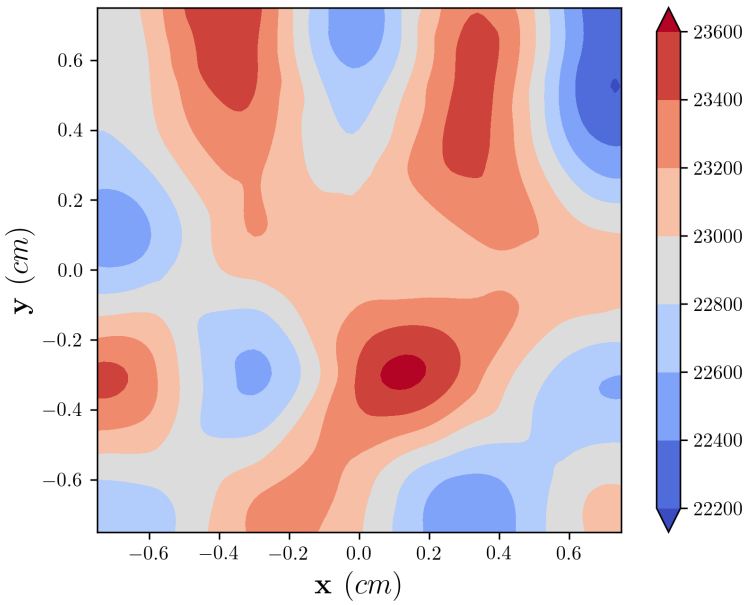

Fig. 3.15 Spatial distribution of the number of (n,α) reactions in the region $0.0112cm < z < 0.0116$.

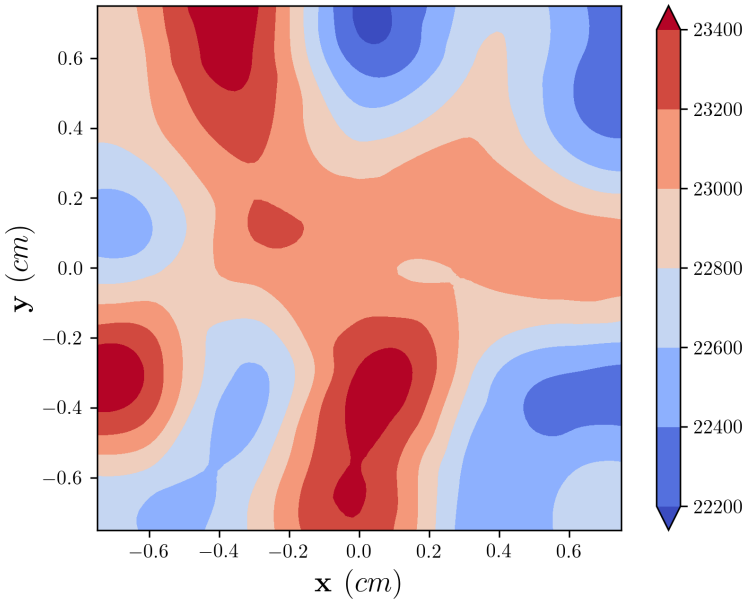

Fig. 3.16 Spatial distribution of the number of (n,α) reactions in the region $0.0116cm < z < 0.0120$.

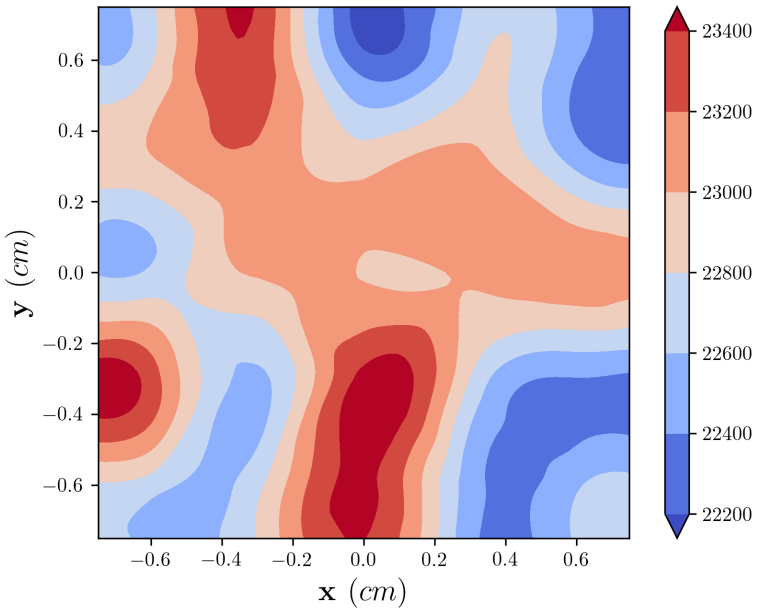

Fig. 3.17 Spatial distribution of the number of (n,α) reactions in the region $0.0120cm < z < 0.0124$.

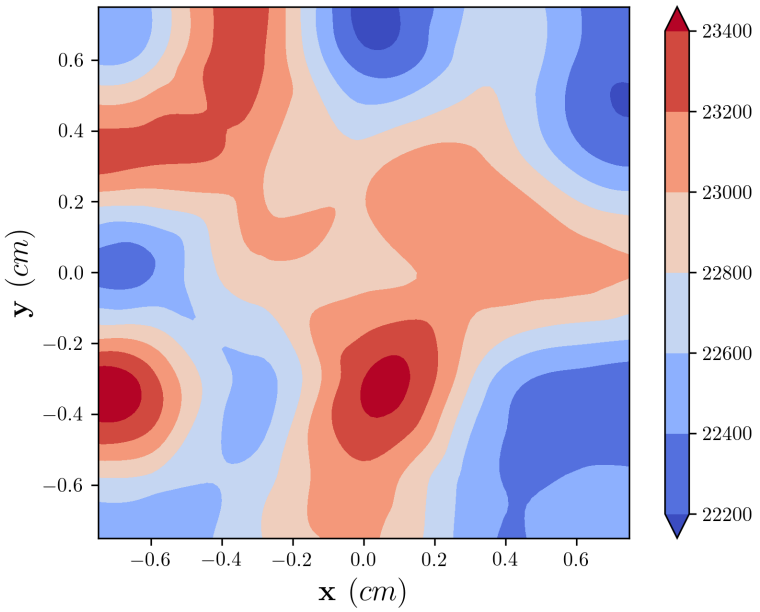

Fig. 3.18 Spatial distribution of the number of (n,α) reactions in the region $0.0124cm < z < 0.0128$.

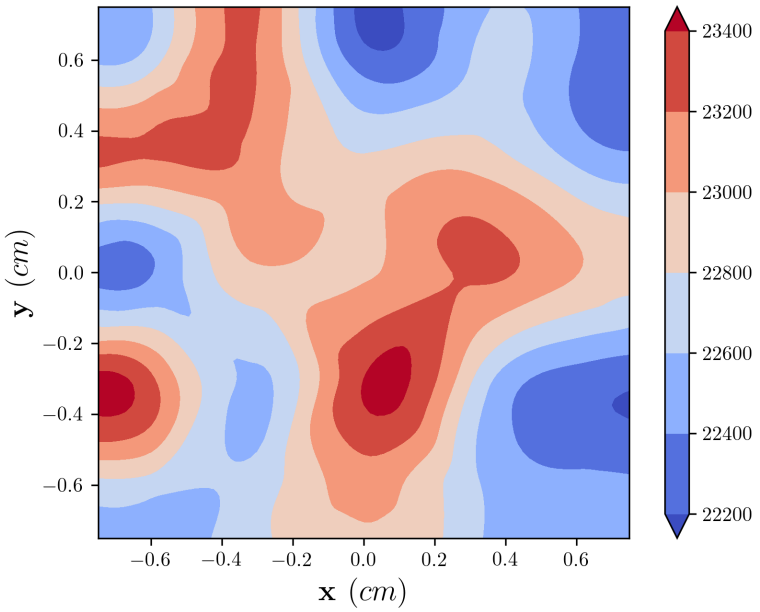

Fig. 3.19 Spatial distribution of the number of (n,α) reactions in the region $0.0128cm < z < 0.0132$.

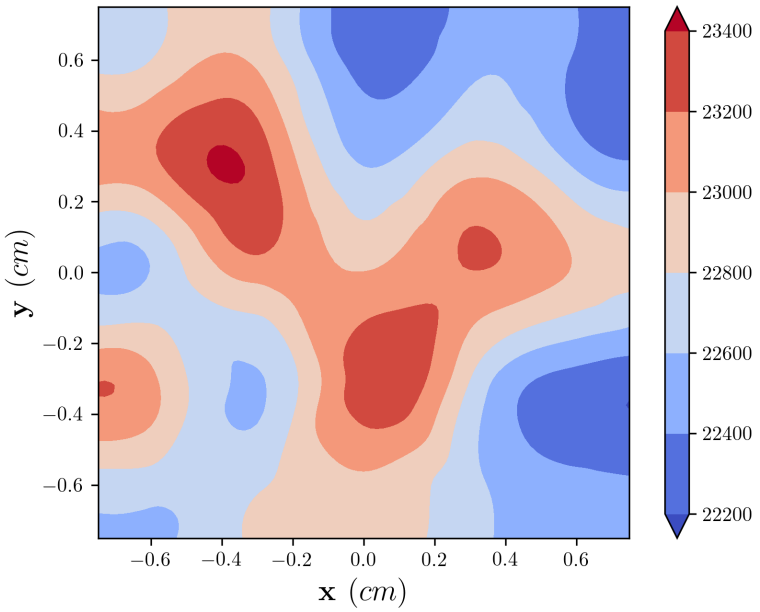

Fig. 3.20 Spatial distribution of the number of (n,α) reactions in the region $0.0132cm < z < 0.0136$.

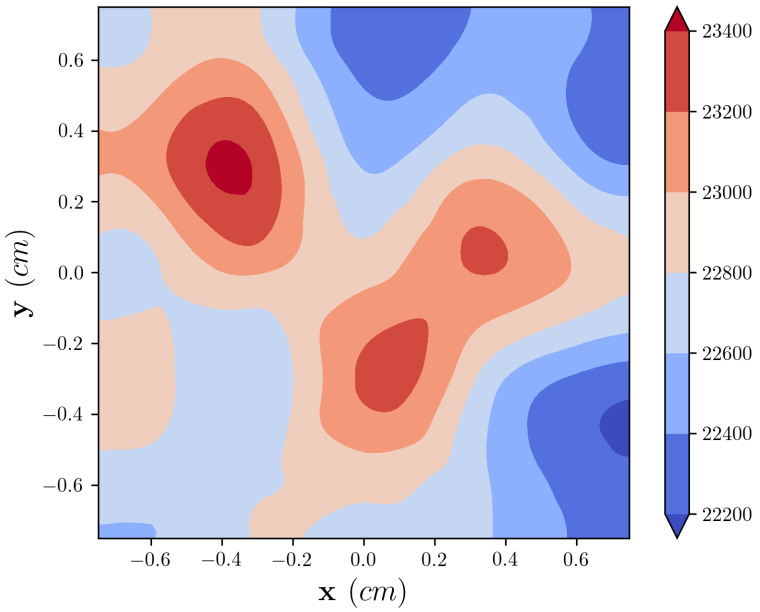

Fig. 3.21 Spatial distribution of the number of (n,α) reactions in the region $0.0136cm < z < 0.0140$.

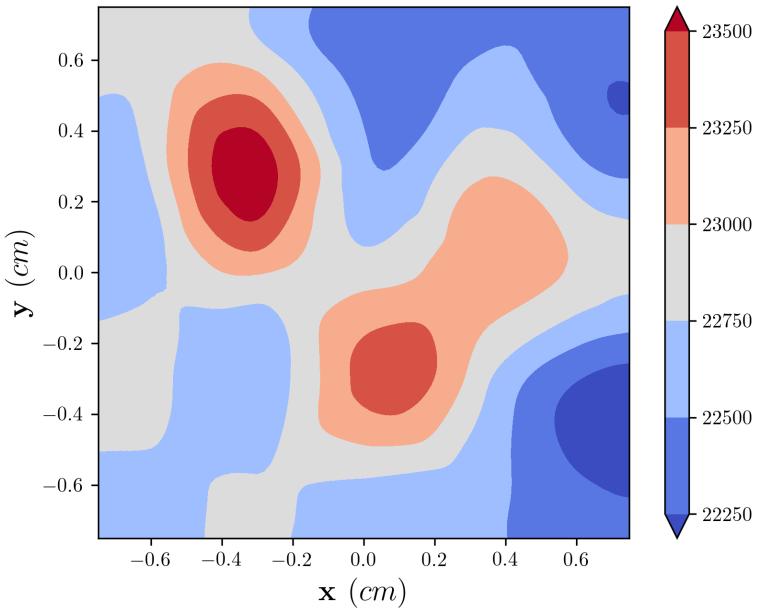

Fig. 3.22 Spatial distribution of the number of (n,α) reactions in the region $0.0140cm < z < 0.0144$.

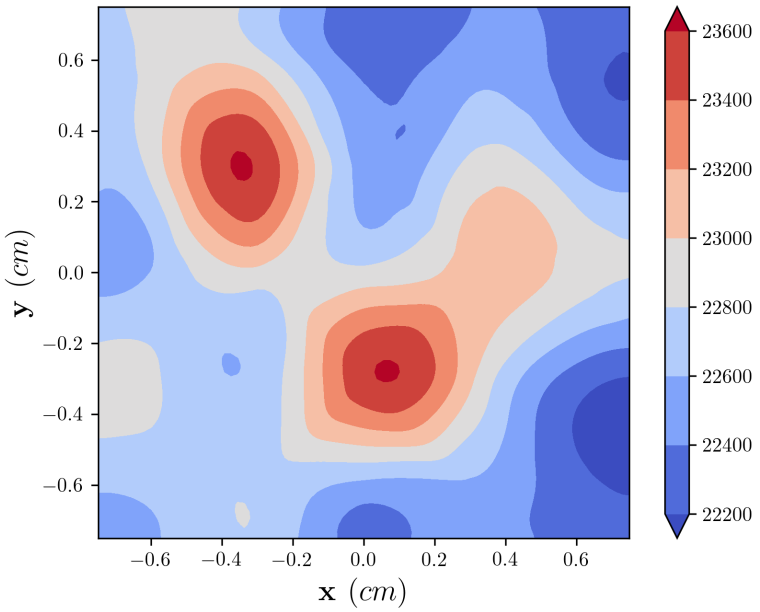

Fig. 3.23 Spatial distribution of the number of (n, α) reactions in the region $0.0144cm < z < 0.0148$.

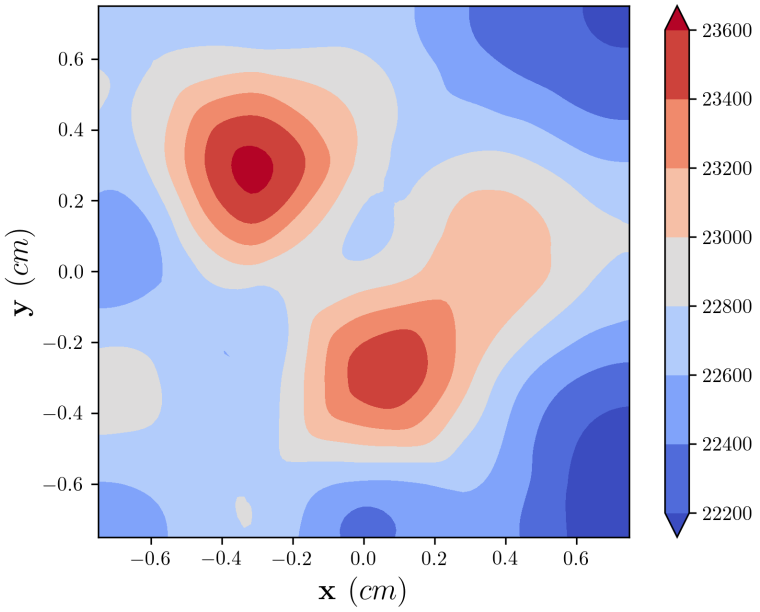

Fig. 3.24 Spatial distribution of the number of (n, α) reactions in the region $0.0148cm < z < 0.0152$.

The spatial distribution of the number of alpha particles from (n,α) reaction do not follow a uniform distribution, but they are mainly concentrated in the centre. By adopting the given distribution into Appendix B, we can estimate the number of alpha particles that reach the detector surface generating visible tracks. We also use the four different V functions aforementioned to select alpha particle from the detector surface that generates visible tracks, as shown in Table. 3.2.

Table 3.2 The number of visible tracks in detector surface depending on the V function from Table. 2.3.

V function	The number of visible tracks
A[63]	1
B[64]	0
C[65]	0
D[66]	0

It is observed that the efficiency is equal zero when using LR-115 detectors. Because an alpha particle of $1.47MeV$ and $1.78MeV$ travels through the natural boron a total distance of $0.00034267cm$ and $0.00042956MeV$, respectively. These small distances indicate that there is a small probability that an alpha particle can reach the detector surface with a value of 1.61%. Besides, the LR-115 also has a narrow energy window, even when using different V functions as shown in Fig. 2.8, this decreases the probability much more with values close to 0. So, only the first V function reach an efficiency equal to 9.80×10^{-8}.

In this case, we can improve it by using the CR-39 because it has a wide energy window. In other words, the CR-39 will detect more alpha particles from (n,α) reactions than the LR-115. The CR-39 detector registers 16046 ± 193 visible tracks in an area of $(1.5\times1.5)cm^2$ at the same conditions. So, the efficiency is equal $1.57\times10^{-3}\pm1.54\times10^{-10}$.

3.3 Detectors exposed to radon and thoron progenies

Radon or thoron progenies can be measured by placing an absorbent film, such as mylar, over the detector. However, alpha particles are not emitted inside the film, as in the previous section, because progenies are deposited onto the film's surface and emit alpha particles there. This detection method is well known as DRPS and DTPS for measuring radon and thoron progeny, respectively [54, 56]. We can assume that the radon or thoron progenies are deposited uniformly in the mylar surface for simplicity. Using the algorithm from

Appendix B, we estimate the efficiency of LR-115 to radon/thoron progeny. For radon progeny, we can use mylar with a thickness of $37\mu m$. Considering this thickness, we can see that the ^{214}Bi can not penetrate it and ^{218}Po atoms penetrate the mylar film in a very small percentage. Besides, the ^{214}Po can also reach the detector surface. Table. 3.3 shows the total range for each radon progeny in order to numerically verify this.

Table 3.3 Total travelling distance of an alpha particle emitted by ^{218}Po, ^{214}Bi or ^{214}Po in the mylar.

Nuclides	Total range in mylar $[\mu m]$
$^{218}Po[6.00235MeV]$	37.2497
$^{214}Bi[5.516MeV]$	32.7206
$^{214}Po[7.68682MeV]$	55.0340

For thoron progeny, we can use a mylar of $50\mu m$, where only ^{212}Po reach the detector surface. We can compare the total ranges of thoron progenies in Table. 3.4.

Table 3.4 Total travelling distance of an alpha particle emitted by ^{216}Po, ^{212}Bi or ^{212}Po in the mylar.

Nuclides	Total range in mylar $[\mu m]$
$^{216}Po[6.7784MeV]$	45.0394
$^{212}Bi[6.05104MeV]$	37.7182
$^{212}Po[8.78517MeV]$	68.3048

Then, the efficiency of LR-115 to radon/thoron progeny in both DRPS and DTPS was calculated as shown in Table. 3.5.

Table 3.5 Track registration efficiencies of radon and thoron progeny in DRPS and DTPS.

	Efficiency
$\eta_{DRPS,radon}$	$0.0683 \pm 0.0005 \times 10^{-2}$
$\eta_{DRPS,thoron}$	0.0122 ± 0.0001
$\eta_{DTPS,radon}$	close to 0
$\eta_{DTPS,thoron}$	0.0813 ± 0.0047

where $\eta_{DRPS,radon}$ is the efficiency of radon progeny in DRPS, $\eta_{DRPS,thoron}$ is the efficiency of thoron progeny in DRPS, $\eta_{DTPS,radon}$ is the efficiency of radon progeny in DTPS and $\eta_{DTPS,thoron}$ is the efficiency of thoron progeny in DTPS. Results from Table. 3.5 are comparable with other authors [124, 54, 125].

Chapter 4

Conclusions and future outlooks

The entire thesis corresponds to a compendium of research papers proposed and executed during the doctorate.

4.1 Conclusions

- A methodology was developed to estimate the response, or calibration factor, of the LR-115 detector exposed inside a non-commercial-conductive cylindrical diffusion chamber, using unconventional Monte Carlo methods which show more realistic results because they imitate the experimental procedure used in estimating the calibration factor. This methodology was also compared and with the conventional Monte Carlo methods used by several authors, being both in good agreement. However, when using the methodology with very high radon exposure levels, the detector response was affected.

- This methodology took into account the radon exposure, air density, type of entry, diffusion chamber material and dimensions, an etching process, and a readout procedure. These parameters were necessary to obtain more realistic results of the detector response, since several authors estimate the detector response only taking into account the dimensions of the diffusion chamber and the V function. Results from this methodology also was in good agreement with the experimental outcomes.

- According to [72], we also showed that the calibration factor between a conductive and non-conductive diffusion chamber was not change significantly. So the diffusion chamber material does not influence at all when calculating the calibration factor, especially when estimating the fraction of ^{218}Po atoms deposited on the internal walls of the chamber.

- It was noted that one of the limitations of the methodology for estimating detector response was the dependence of the overlapping effect that affects the detector response giving overestimated values, or simply wrong values. This effect can be seen when detectors are exposed under very high exposures. Therefore, the overlapping effect was studied by building a model that can correct the influence of the overlapped tracks with an uncertainty of 5%.

- Nuclear track detectors exposed in unconventional bare mode were studied by exposing them to natural outdoor radiation. Results showed that UV radiation could not only degrade the LR-115 detector when its active layer is exposed to natural outdoor radiation, but that can also generate concentric tracks when the non-active layer is exposed to this radiation. This very particular optical phenomenon was studied in other polymers, but as far as we know, there are no studies applied to LR-115.

- The methodology from Appendix B really comes in handy to estimate the efficiency of detectors covered by converters or absorbers. The efficiency was calculated by using simulation and results are in good agreement with other authors.

4.2 Future outlooks

- The methodology used was only applied to LR-115 detectors in a diffusion chamber. However, we are going to apply this to various nuclear track detectors, not only to measure radon concentration but also to measure only thoron in a diffusion chamber. Since several authors measure the thoron concentration by using twin chamber, where it has two compartments that measure radon + thoron and only radon. According to this, we are going to use our proposed methodology to built a device that measure only thoron using a single compartment (diffusion chamber).

- In the Section 3.3, we estimated the efficiency of the detector covered by converters or absorbers. So, we propose to optimize the efficiency of the detector by making a complete study with different absorbers or converters taking into account their thickness and the form of deposition in the detector.

References

[1] Guy D Coughlan and James Edmund Dodd. *The ideas of particle physics: an introduction for scientists*. Cambridge University Press, 1991.

[2] Alinka Lépine-Szily and Pierre Descouvemont. Nuclear astrophysics: nucleosynthesis in the universe. *International Journal of Astrobiology*, 11(4):243, 2012.

[3] Dennis Silverman et al. A modern introduction to particle physics. *PhT*, 47(1):48, 1994.

[4] B.K. Bhaumik. Radioactivity. this article is written for earth science students who intend to take a course on crustal radioactivity., may 2014.

[5] PW Swarzenski. U/th series radionuclides as coastal groundwater tracers. *Chemical Reviews*, 107(2):663–674, 2007.

[6] UNSCEAR. Sources and effects of ionizing radiation. Technical report, United Nations Scientific Committee on the Effects of Atomic Radiation, 2000.

[7] MW Charles. Radon exposure of the skin: I. biological effects. *Journal of Radiological Protection*, 27(3):231, 2007.

[8] Philip K Hopke. Some thoughts on the" unattached" fraction of radon decay products. *Health physics*, 63(2):209–212, 1992.

[9] National Research Council et al. *Comparative dosimetry of radon in mines and homes*. National Academies Press, 1991.

[10] J Miles. Methods of radon measurement and devices. In *Proceedings of the 4th European conference on protection against radon at home and at work Conference programme and session presentations, Czech Republic*, 2004.

[11] John F DeWild and James T Krohelski. *Radon-222 Concentrations in Ground Water and Soil Gas on Indian Reservations in Wisconsin*, volume 95. US Department of the Interior, US Geological Survey, 1995.

[12] A Abbady, Adel GE Abbady, and Rolf Michel. Indoor radon measurement with the lucas cell technique. *Applied Radiation and Isotopes*, 61(6):1469–1475, 2004.

[13] Meleq Bahtijari, Peter Stegnar, Zahadin Shemsidini, H Ajazaj, Y Halimi, Janja Vaupotič, and Ivan Kobal. Seasonal variation of indoor air radon concentration in schools in kosovo. *Radiation measurements*, 42(2):286–289, 2007.

[14] Jovana Nikolov, Ivana Stojković, Nataša Todorović, Branislava Tenjović, Srđan Vuković, and Jovana Knežević. Evaluation of different lsc methods for 222rn determination in waters. *Applied Radiation and Isotopes*, 142:56–63, 2018.

[15] GM Shilpa, BN Anandaram, and TL Mohankumari. Measurement of 222rn concentration in drinking water in the environs of thirthahalli taluk, karnataka, india. *Journal of radiation research and applied sciences*, 10(3):262–268, 2017.

[16] J Bigu. Improved 220rn measurement characteristics of scintillation cells cooled to liquid nitrogen temperatures. *Applied radiation and isotopes*, 44(6):949–955, 1993.

[17] KP Eappen, BK Sapra, and YS Mayya. A novel methodology for online measurement of thoron using lucas scintillation cell. *Nuclear Instruments and Methods in Physics Research Section A: Accelerators, Spectrometers, Detectors and Associated Equipment*, 572(2):922–925, 2007.

[18] KP Eappen, RN Nair, and YS Mayya. Simultaneous measurement of radon and thoron using lucas scintillation cell. *Radiation measurements*, 43(1):91–97, 2008.

[19] Akihiro Sakoda, Oliver Meisenberg, and Jochen Tschiersch. An approach to discriminatively determine thoron and radon emanation rates for a granular material with a scintillation cell. *Radiation Measurements*, 89:8–13, 2016.

[20] P Baltzer, KG Görsten, and A Bäcklin. A pulse-counting ionization chamber for measuring the radon concentration in air. *Nuclear Instruments and Methods in Physics Research Section A: Accelerators, Spectrometers, Detectors and Associated Equipment*, 317(1-2):357–364, 1992.

[21] F Roessler, W Buerkin, and J Villert. Alphaguard, the new reference for continuous radon monitoring in air, soil, gas, water and material.

[22] C Ferry, A Beneito, P Richon, and M-C Robe. An automatic device for measuring the effect of meteorological factors on radon-222 flux from soils on the long term. *Radiation protection dosimetry*, 93(3):271–274, 2001.

[23] HS Virk, Kumar Naresh, Navjeet Sharma, and BS Bajwa. Alpha-guard radon survey in soil-gas and dwellings of some uranium-rich areas of himachal pradesh, india. *Current Science (Bangalore)*, 75(5):430–431, 1998.

[24] Christopher YH Chao, Thomas CW Tung, and John Burnett. Influence of ventilation on indoor radon level. *Building and Environment*, 32(6):527–534, 1997.

[25] PM Kolarž, DM Filipović, and BP Marinković. Daily variations of indoor air-ion and radon concentrations. *Applied Radiation and Isotopes*, 67(11):2062–2067, 2009.

[26] J Planinic, Zdravko Faj, Vanja Radolić, Goran Šmit, and Dario Faj. Indoor radon dose assessment for osijek. *Journal of environmental radioactivity*, 44(1):97–106, 1999.

[27] Janine Nicolosi Corrêa, Sergei A Paschuk, Hugo R Schelin, Laercio Barbosa, Tatyana Sadula, and Cristiana A Matsuzaki. Measurements of radon concentration levels in drinking water at urban area of curitiba, brazil. 2009.

[28] Natasa Todorovic, Jovana Nikolov, Sofija Forkapic, Istvan Bikit, Dusan Mrdja, Miodrag Krmar, and Miroslav Veskovic. Public exposure to radon in drinking water in serbia. *Applied Radiation and Isotopes*, 70(3):543–549, 2012.

[29] Elzbieta Kochowska, Krzysztof Kozak, Beata Kozłowska, Jadwiga Mazur, and Jerzy Dorda. Test measurements of thoron concentration using two ionization chambers alphaguard vs. radon monitor rad7. *Nukleonika*, 54:189–192, 2009.

[30] Weihai Zhuo, Shinji Tokonami, Hidenori Yonehara, and Yuji Yamada. A simple passive monitor for integrating measurements of indoor thoron concentrations. *Review of scientific instruments*, 73(8):2877–2881, 2002.

[31] Sami H Alharbi and Riaz A Akber. Radon-222 activity flux measurement using activated charcoal canisters: Revisiting the methodology. *Journal of environmental radioactivity*, 129:94–99, 2014.

[32] N Karunakara, K Sudeep Kumara, I Yashodhara, BK Sahoo, JJ Gaware, BK Sapra, and YS Mayya. Evaluation of radon adsorption characteristics of a coconut shell-based activated charcoal system for radon and thoron removal applications. *Journal of environmental radioactivity*, 142:87–95, 2015.

[33] Andrey Tsapalov, Konstantin Kovler, and Peter Miklyaev. Open charcoal chamber method for mass measurements of radon exhalation rate from soil surface. *Journal of environmental radioactivity*, 160:28–35, 2016.

[34] WM Arafa, H Alneimi, L Al-Houty, and H Abou-Leila. Some improvements of charcoal measurement techniques used for indoor radon measurements in qatar. *Radiation Physics and Chemistry*, 44(1-2):237–240, 1994.

[35] P Kotrappa, T Brubaker, JC Dempsey, and LR Stieff. Electret ion chamber system for measurement of environmental radon and environmental gamma radiation. *Radiation Protection Dosimetry*, 45(1-4):107–110, 1992.

[36] D Nikezic, D Krstic, and S Savovic. Response of diffusion chamber with lr115 detector and electret to radon and progeny. *Radiation measurements*, 44(9-10):783–786, 2009.

[37] RH Mahat, DA Bradley, YM Amin, CY Wong, and LD Su. The effect of humidity on the accuracy of measurement of an electret radon dosimeter. *Radiation Physics and Chemistry*, 61(3-6):489–490, 2001.

[38] Atsuyuki Sorimachi, Hiroyuki Takahashi, and Shinji Tokonami. Influence of the presence of humidity, ambient aerosols and thoron on the detection responses of electret radon monitors. *Radiation Measurements*, 44(1):111–115, 2009.

[39] R Shweikani, M Ka'aka, and R Bardan. Charginge-perm for radon measurements. *Radiation measurements*, 62:10–14, 2014.

[40] Abdulrahman S Alghamdi, Khalid A Aleissa, and Ibrahim F Al-Hamarneh. Gamma radiation and indoor radon concentrations in the western and southwestern regions of saudi arabia. *Heliyon*, 5(1):e01133, 2019.

[41] Anthony R Denman, Chris J Groves-Kirkby, Paul S Phillips, Robin GM Crockett, A Woolridge, and Gavin K Gillmore. The practical use of electrets in a public health radon remediation campaign. *Journal of environmental radioactivity*, 84(3):375–391, 2005.

[42] G Knop and W Paul. Interaction of electrons and α-particles with matter. In *Alpha-, beta-and gamma-ray spectroscopy*, pages 1–36. Elsevier, 1968.

[43] AL Frank and EV Benton. A diffusion chamber radon dosimeter for use in mine environment. *Nuclear Instruments and Methods*, 109(3):537–539, 1973.

[44] Robert Louis Fleischer, Paul Buford Price, Robert M Walker, and Robert Mowbray Walker. *Nuclear tracks in solids: principles and applications*. Univ of California Press, 1975.

[45] C Gericke, R Ghose, G Jönsson, K Freyer, H-C Treutler, and W Enge. The calibration of the solid state nuclear track detector lr 115 for radon measurements. *Radiation measurements*, 31(1-6):363–366, 1999.

[46] Dragoslav Nikezic, KN Yu, and JM Stajic. Computer program for the sensitivity calculation of a cr-39 detector in a diffusion chamber for radon measurements. *Review of Scientific Instruments*, 85(2):022102, 2014.

[47] Jorge Rickards, Jose-Ignacio Golzarri, and Guillermo Espinosa. A monte carlo study of radon detection in cylindrical diffusion chambers. *Journal of environmental radioactivity*, 101(5):333–337, 2010.

[48] Octavian Sima. Monte carlo simulation of radon ssnt detectors. *Radiation measurements*, 34(1-6):181–186, 2001.

[49] JM Stajic, B Milenkovic, and D Nikezic. Study of cr-39 and makrofol efficiency for radon measurements. *Radiation Measurements*, 117:19–23, 2018.

[50] H Papaefthymiou and CD Georgiou. Indoor radon levels in primary schools of patras, greece. *Radiation protection dosimetry*, 124(2):172–176, 2007.

[51] Josip Planinić, Goran Šmit, Zdravko Faj, Božica Šuveljak, Branko Vuković, and Vanja Radolić. Radon in schools and dwellings of osijek. *Journal of radioanalytical and nuclear chemistry*, 191(1):45–51, 1995.

[52] Lutfi Majeed Mohammed Salih. Measurement of radon concentrations and annual dose rate in some regions of baghdad city using lr-115 nuclear track detector. *Al-Nahrain Journal of Science*, 17(3):94–98, 2014.

[53] F Castillo, G Espinosa, JI Golzarri, D Osorio, J Rangel, PG Reyes, and JJE Herrera. Fast neutron dosimetry using cr-39 track detectors with polyethylene as radiator. *Radiation Measurements*, 50:71–73, 2013.

[54] Mukesh Prasad, Mukesh Rawat, Anoop Dangwal, Manjulata Yadav, GS Gusain, Rosaline Mishra, and RC Ramola. Measurements of radon and thoron progeny concentrations in dwellings of tehri garhwal, india, using lr-115 deposition-based dtps/drps technique. *Radiation protection dosimetry*, 167(1-3):102–106, 2015.

[55] N Sinenian, MJ Rosenberg, M Manuel, SC McDuffee, DT Casey, AB Zylstra, HG Rinderknecht, M Gatu Johnson, FH Séguin, JA Frenje, et al. The response of cr-39 nuclear track detector to 1–9 mev protons. *Review of Scientific Instruments*, 82(10):103303, 2011.

[56] Zora S Žunić, Rosaline Mishra, Igor Čeliković, Zdenka Stojanovska, Ilia V Yarmoshenko, Georgy Malinovsky, Nenad Veselinović, Ljiljana Gulan, Zoran Ćurguz, Janja Vaupotič, et al. Effective doses estimated from the results of direct radon and thoron progeny sensors (drps/dtps), exposed in selected regions of balkans. *Radiation protection dosimetry*, 185(3):387–390, 2019.

[57] S Djeffal, Z Lounis, and M Allab. Design of a radon measuring device based on the diffusion principle using lr 115 detector. *Radiation measurements*, 28(1-6):629–632, 1997.

[58] BK Sahoo, BK Sapra, SD Kanse, JJ Gaware, and YS Mayya. A new pin-hole discriminated 222rn/220rn passive measurement device with single entry face. *Radiation Measurements*, 58:52–60, 2013.

[59] Shinji Tokonami, Hiroyuki Takahashi, Yosuke Kobayashi, Weihai Zhuo, and Erik Hulber. Up-to-date radon-thoron discriminative detector for a large scale survey. *Review of Scientific Instruments*, 76(11):113505, 2005.

[60] W "Zhang, K Ungar, J Chen, N St-Amant, and B" Tracy. An accurate method for the determination of 226ra activity concentrations in soil. *Journal of radioanalytical and nuclear chemistry*, 280(3):561–567, 2009.

[61] A Picard and H Fang. Three methods of determining the density of moist air during mass comparisons. *Metrologia*, 39(1):31, 2002.

[62] James F Ziegler, Matthias D Ziegler, and Jochen P Biersack. Srim–the stopping and range of ions in matter (2010). *Nuclear Instruments and Methods in Physics Research Section B: Beam Interactions with Materials and Atoms*, 268(11-12):1818–1823, 2010.

[63] Saeed A Durrani and Richard K Bull. *Solid state nuclear track detection: principles, methods and applications*, volume 111. Elsevier, 2013.

[64] SA Durrani and PF Green. The effect of etching conditions on the response of lr115. *Nuclear Tracks and Radiation Measurements (1982)*, 8(1-4):21–24, 1984.

[65] R Barillon, M Fromm, A Chambaudet, H Marah, and A Sabir. Track etch velocity study in a radon detector (lr 115, cellulose nitrate). *Radiation measurements*, 28(1-6):619–628, 1997.

[66] SYY Leung, D Nikezic, and KN Yu. Derivation of v function for lr 115 ssntd from its partial sensitivity to 222rn and its short-lived progeny. *Journal of environmental radioactivity*, 92(1):55–61, 2007.

[67] Dragoslav Nikezic and KN Yu. Computer program track_test for calculating parameters and plotting profiles for etch pits in nuclear track materials. *Computer Physics Communications*, 174(2):160–165, 2006.

[68] Lenore Blum, Manuel Blum, and Mike Shub. A simple unpredictable pseudo-random number generator. *SIAM Journal on computing*, 15(2):364–383, 1986.

[69] William B Langdon. A fast high quality pseudo random number generator for nvidia cuda. In *Proceedings of the 11th Annual Conference Companion on Genetic and Evolutionary Computation Conference: Late Breaking Papers*, pages 2511–2514, 2009.

[70] Shinya Maehara, Kohei Kawakami, Hideaki Arai, Kenji Nakano, Kohei Doi, Takashi Sato, Yasuo Ohdaira, Shuichi Sakamoto, and Masashi Ohkawa. Frequency noise characteristics of a diode laser and its application to physical random number generation. *Optical Engineering*, 52(1):014302, 2013.

[71] TR Beck, H Buchröder, E Foerster, and V Schmidt. Interlaboratory comparisons for passive radon measuring devices at bfs. *Radiation protection dosimetry*, 125(1-4):572–575, 2007.

[72] D Nikezić and N Stevanović. Radon progeny behavior in diffusion chamber. *Nuclear Instruments and Methods in Physics Research Section B: Beam Interactions with Materials and Atoms*, 239(4):399–406, 2005.

[73] D Pressyanov, I Rusinov, and G Simeonov. Radon progeny deposition in track-detection diffusion chambers. *Nuclear Instruments and Methods in Physics Research Section A: Accelerators, Spectrometers, Detectors and Associated Equipment*, 435(3):509–513, 1999.

[74] VSY Koo, CWY Yip, JPY Ho, D Nikezic, and KN Yu. Sensitivity of lr115 detector in diffusion chamber to 222rn in the presence of 220rn. *Applied radiation and isotopes*, 56(6):953–956, 2002.

[75] VSY Koo, CWY Yip, JPY Ho, D Nikezic, and KN Yu. Deposition fractions of 218po in diffusion chambers. *Applied radiation and isotopes*, 59(1):49–52, 2003.

[76] JP McLaughlin and B Fitzgerald. Models for determining the response of passive alpha particle detectors to radon and its progeny in cylindrical detecting volumes. *Radiation Protection Dosimetry*, 56(1-4):241–246, 1994.

[77] Dobromir S Pressyanov. Radon progeny distribution in cylindrical diffusion chambers. *Nuclear Instruments and Methods in Physics Research Section A: Accelerators, Spectrometers, Detectors and Associated Equipment*, 596(3):446–450, 2008.

[78] KP Eappen and YS Mayya. Calibration factors for lr-115 (type-ii) based radon thoron discriminating dosimeter. *Radiation measurements*, 38(1):5–17, 2004.

[79] D Palacios, L Sajo-Bohus, and ED Greaves. Radon progeny distributions inside a diffusion chamber and their contributions to track density in ssnt detectors. *Radiation measurements*, 40(2-6):657–661, 2005.

[80] Donald L Ermak and Helen Buckholz. Numerical integration of the langevin equation: Monte carlo simulation. *Journal of Computational Physics*, 35(2):169–182, 1980.

[81] Don S Lemons and Anthony Gythiel. Paul langevin's 1908 paper "on the theory of brownian motion"["sur la théorie du mouvement brownien," cr acad. sci.(paris) 146, 530–533 (1908)]. *American Journal of Physics*, 65(11):1079–1081, 1997.

[82] Sune Jespersen, Ralf Metzler, and Hans C Fogedby. Lévy flights in external force fields: Langevin and fractional fokker-planck equations and their solutions. *Physical Review E*, 59(3):2736, 1999.

[83] Mark P Silverman. Brownian motion of decaying particles: Transition probability, computer simulation, and first-passage times. *Journal of Modern Physics*, 8:1809, 2017.

[84] William W Nazaroff and Anthony V Nero. Radon and its decay products in indoor air. 1988.

[85] George EP Box. A note on the generation of random normal deviates. *Ann. Math. Statist.*, 29:610–611, 1958.

[86] D Palacios, L Sajó-Bohus, H Barros, ED Greaves, and F Palacios. Alternative method to determine the bulk etch rate of lr-115 detectors. *Revista Mexicana de Física*, 56(1):22–25, 2010.

[87] Debajyoti Barooah and Sarat Phukan. Study of subsoil radon anomaly using lr-115 (ii) nuclear track detectors in and around the geleki oilfield, assam shelf. *Indian Journal of Physics*, 86(9):801–805, 2012.

[88] G Jönsson. Solid state nuclear track detectors in radon measurements indoors and in the soil. *International Journal of Radiation Applications and Instrumentation. Part D. Nuclear Tracks and Radiation Measurements*, 19(1-4):335–338, 1991.

[89] Nisha Mann, Amit Kumar, Sushil Kumar, and Rishi Pal Chauhan. Radon-thoron measurements in air and soil from some districts of northern part of india. *Nuclear Technology and Radiation Protection*, 30(4):294–300, 2015.

[90] SM Nasser, Mayeen Uddin Khandaker, David Andrew Bradley, and Matthew Omoniyi Isinkaye. Evaluation of radon concentration in irrigation and drinking waters from the eastern part of oman and estimation of effective doses to omanis. *Radiation protection dosimetry*, 184(3-4):422–425, 2019.

[91] Surinder Singh, Rohit Mehra, and Kulwant Singh. Seasonal variation of indoor radon in dwellings of malwa region, punjab. *Atmospheric Environment*, 39(40):7761–7767, 2005.

[92] R Rabi and L Oufni. Study of radon dispersion in typical dwelling using cfd modeling combined with passive-active measurements. *Radiation Physics and Chemistry*, 139:40–48, 2017.

[93] B Burghele, A Ţenter, A Cucoş, T Dicu, M Moldovan, B Papp, K Szacsvai, T Neda, L Suciu, A Lupulescu, et al. The first large-scale mapping of radon concentration in soil gas and water in romania. *Science of the Total Environment*, 669:887–892, 2019.

[94] G Cinelli, L Tositti, B Capaccioni, E Brattich, and D Mostacci. Soil gas radon assessment and development of a radon risk map in bolsena, central italy. *Environmental geochemistry and health*, 37(2):305–319, 2015.

[95] Lazaro Luis Vilcapoma, María Elena López Herrera, Patrizia Pereyra, Daniel Francisco Palacios, Bertin Pérez, Jhonny Rojas, and Laszlo Sajo-Bohus. Measurement of radon in soils of lima city-peru during the period 2016-2017. *Earth Sciences Research Journal*, 23(3), 2019.

[96] Francesca Giustini, Giancarlo Ciotoli, Alessio Rinaldini, Livio Ruggiero, and Mario Voltaggio. Mapping the geogenic radon potential and radon risk by using empirical

bayesian kriging regression: A case study from a volcanic area of central italy. *Science of the Total Environment*, 661:449–464, 2019.

[97] Phong Thu Huynh Nguyen, Ngoc Ba Vu, Hao Le Cong, et al. Soil radon gas in some soil types in the rainy season in ho chi minh city, vietnam. *Journal of environmental radioactivity*, 193:27–35, 2018.

[98] RC Ramola, Yogesh Prasad, Ganesh Prasad, Sushil Kumar, and VM Choubey. Soil-gas radon as seismotectonic indicator in garhwal himalaya. *Applied Radiation and Isotopes*, 66(10):1523–1530, 2008.

[99] GS Gusain, Ganesh Prasad, Yogesh Prasad, and RC Ramola. Comparison of indoor radon level with radon exhalation rate from soil in garhwal himalaya. *Radiation measurements*, 44(9-10):1032–1035, 2009.

[100] Janja Vaupotič, Igor Čeliković, Nataša Smrekar, Zora S Žunić, and Ivan Kobal. Concentrations of 222 rn and 220 rn in indoor air. *Acta Chimica Slovenica*, 55(1), 2008.

[101] Yu V Stenkin, VV Alekseenko, DM Gromushkin, OB Shchegolev, and VP Sulakov. Barometric pumping effect for radon-due neutron flux in underground laboratories. *arXiv preprint arXiv:1605.01283*, 2016.

[102] F Leonardi, Marco Caresana, M D'Alessandro, R Mishra, S Tonnarini, R Trevisi, and M Veschetti. An extended study of the etching characteristics of cr-39 detectors. *Radiation Measurements*, 44(9-10):787–790, 2009.

[103] D Palacios, L Sajo-Bohus, H Barros, E Fusella, and Y Avila. Analysis and correction of track overlapping on nuclear track detectors (ssntd). *Revista mexicana de física*, 57:34–39, 2011.

[104] Karel Turek, Metody Gelev, and Iancho Dimov. Comparative measurements of soil gas radon concentration using thermoluminescent and track detectors. *Radiation measurements*, 38(4-6):843–846, 2004.

[105] DT Clark and PJ Stephenson. Electron-spectroscopy for chemical applications (esca) applied to polymers-an esca study of the surface-chemistry of cellulose nitrates and double based propellants, with particular reference to their degradation in uv-light. *POLYMER DEGRADATION AND STABILITY*, 4(3):185–193, 1982.

[106] Vaibhav Kulshrestha, Garima Agarwal, Kamlendra Awasthi, Devendra Vyas, and YK Vijay. Microscopic studies of electron and ion irradiated polymeric films. *Microscopy: Science, Technology, Applications and Education, Formatex Research Center, Barcelona*, pages 1696–1703, 2010.

[107] AHK Fowler, HS Munro, and DT Clark. Esca studies of the thermal and x-ray induced degradation of cellulose nitrates. *Polymer degradation and stability*, 11(4):287–296, 1985.

[108] S Mayaki, AO Dasilva, and A Tidjani. Effects of gamma irradiation on cellulose nitrate lr 115 type ii. *Radiation measurements*, 26(5):657–661, 1996.

[109] FMF Ng and KN Yu. X-ray irradiation induced degradation of cellulose nitrate. *Materials Chemistry and Physics*, 100(1):38–40, 2006.

[110] Sasha Madronich and Siri Flocke. Theoretical estimation of biologically effective uv radiation at the earth?s surface. In *Solar ultraviolet radiation*, pages 23–48. Springer, 1997.

[111] Eugene V Benton. A study of charged particle tracks in cellulose nitrate. Technical report, NAVAL RADIOLOGICAL DEFENSE LAB SAN FRANCISCO CA, 1968.

[112] Tamon Kusumoto, Yutaka Mori, Masato Kanasaki, Keiji Oda, Satoshi Kodaira, Rémi Barillon, and Tomoya Yamauchi. Drastic decrease of carbonyl group after the loss of ether in padc exposed to 222 nm uv photons. *Radiation Physics and Chemistry*, 157:60–64, 2019.

[113] V Mehta, SP Singh, RP Chauhan, GS Mudahar, et al. Surface chemical etching behavior of lr-115 type ii solid state nuclear track detector: effects of uv and ultrasonic beam. *Optoelectronics and Advanced Materials-Rapid Communications*, 8(9-10):943–947, 2014.

[114] Adams Tidjani. Effects of uv light on the efficiency of alpha-particle detection of cr-39, lr-115 type ii and cn-85. *International Journal of Radiation Applications and Instrumentation. Part D. Nuclear Tracks and Radiation Measurements*, 17(4):491–495, 1990.

[115] Adams Tidjani. Property modifications in uv irradiated polymeric track detectors. *Nuclear Instruments and Methods in Physics Research Section B: Beam Interactions with Materials and Atoms*, 58(1):43–48, 1991.

[116] Taichi Arai, Hiroya Suda, Tetsutaro Igarashi, and Tadamitsu Sakurai. Photoinduced refractive-index change in 4-tert-butylcalix [8] arenes bearing n-acyloxyphenylamide chromophores. *Polymer journal*, 45(2):133–136, 2013.

[117] Thomas Höfler, Thomas Grießer, Xaver Gstrein, Gregor Trimmel, Georg Jakopic, and Wolfgang Kern. Uv reactive polymers for refractive index modulation based on the photo-fries rearrangement. *Polymer*, 48(7):1930–1939, 2007.

[118] Gregor Langer, Thomas Kavc, Wolfgang Kern, Gerald Kranzelbinder, and Eric Toussaere. Refractive index changes in polymers induced by deep uv irradiation and subsequent gas phase modification. *Macromolecular chemistry and physics*, 202(18):3459–3467, 2001.

[119] Yuen-Ron Shen. The principles of nonlinear optics. *New York*, 1984.

[120] Hugh D Young and Roger A Freedman. *University Physics, Volume 2*. Addison-Wesley, 1999.

[121] E Hecht and A Zajac. Optics, ser, 2002.

[122] Michael F L'Annunziata. *Handbook of radioactivity analysis*. Academic press, 2012.

[123] Hector Rene Vega-Carrillo and Segundo Agustín Martinez-Ovalle. Few groups neutron spectra, and dosimetric features, of isotopic neutron sources. *Applied Radiation and Isotopes*, 117:42–50, 2016.

[124] Rosaline Mishra, BK Sapra, and YS Mayya. Multi-parametric approach towards the assessment of radon and thoron progeny exposures. *Review of Scientific Instruments*, 85(2):022105, 2014.

[125] Komal Saini, Parminder Singh, Prabhjot Singh, BS Bajwa, and BK Sahoo. Seasonal variability of equilibrium factor and unattached fractions of radon and thoron in different regions of punjab, india. *Journal of environmental radioactivity*, 167:110–116, 2017.

Appendix A

Simulation of the detector's partial sensitivities to radon isotopes and their progeny.

The alpha particles emitted in the decay of radon and its progeny into the internal volume of the chamber can be registered by following the steps below (using some Python recipes)

Calculation of the travel distance in the air of alpha particles

The stopping power $(-dE/dx)$ of alpha particle in the air (including air density) is given by the SRIM 2013 program (http://www.srim.org). So the energy E_d of an alpha particle after travelling a distance d with initial energy E_i can be computed by solving the equation,

$$d = \int_{E_d}^{E_i} \frac{1}{\left(\frac{dE}{dx}\right)} dE \tag{A.1}$$

This equation can be solved in Python by interpolating $\frac{1}{\left(\frac{dE}{dx}\right)}$ using

```
interpolate.interp1d(x,y,'cubic')
```

then the integral is solved by

```
integrate.simps(y,x)
```

It is possible to calculate the minimum $(Rmin)$ and maximum $(Rmax)$ distances the alpha particle travels from E_i to E_d.

Sampling uniform pseudorandom positions and directions of alpha particles

From now on, we will compute calculations according to this geometrical representation (the red region represents the LR-115 detector u x u cm):

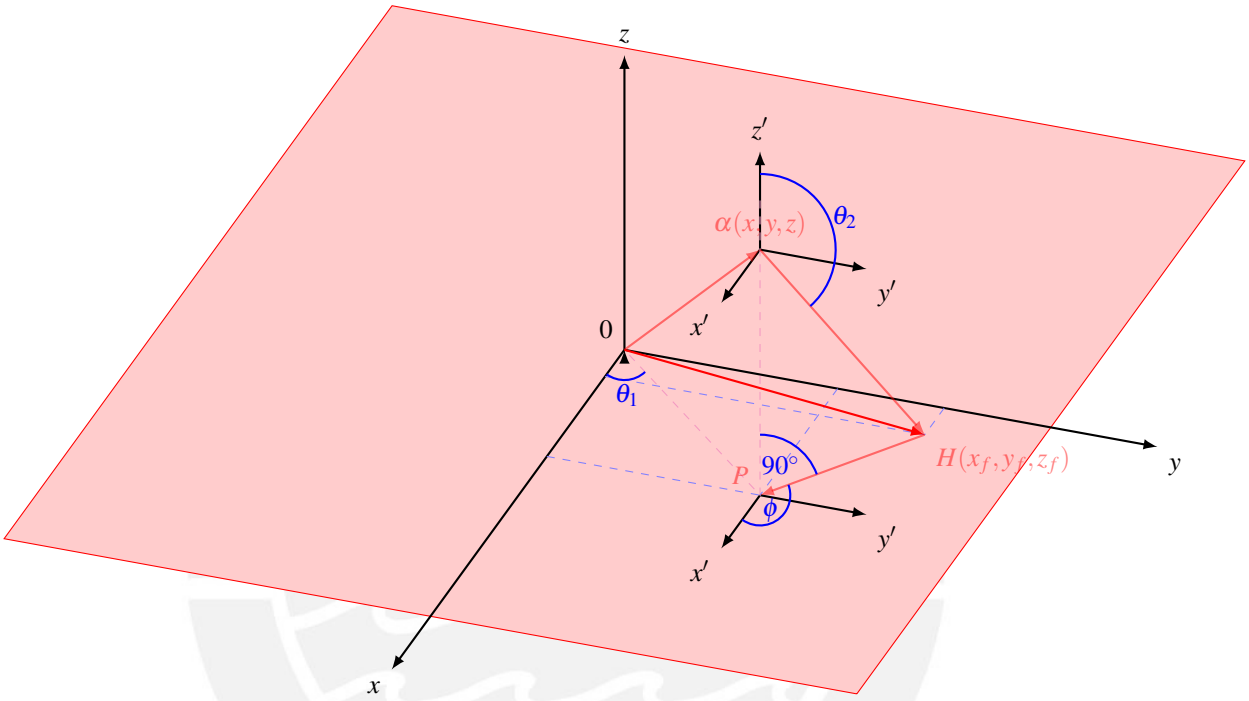

In a case of a cylinder chamber (r_{cy}, h_{cy}), uniform pseudorandom position in cartesian coordinates (x, y, z) for each alpha particle is:

```
radio = r_cy * (random.uniform(0,1))**(1/2)
theta_1 = 2*pi*random.uniform(0,1)
x = radio * cos(theta_1)
y = radio * sin(theta_1)
z = h_cy * random.uniform(0,1)
```

Due to the alpha particles are emitted in an isotropic state, we can express the uniform pseudorandom direction of each alpha particle in spherical coordinates (θ_2, ϕ):

```
cos_theta_2 = -2*random.uniform(0,1) + 1
phi = 2 * pi * random.uniform(0,1)
```

Does an alpha particle reach the detector surface?

It is possible to determine if an alpha particle hit the square detector surface, using the pseudorandom direction of each alpha particle:

```
d_PH = tan(pi - arccos(cos_theta)) * z
x_f = x + cos(fi)*d_PH
y_f = y + sin(fi)*d_PH
d_0H = (x_f ** 2 + y_f ** 2) ** (1/2)
i_angle = degrees(arccos(cos_theta) - (pi/2))  # incident angle
if d_0H < = (((2*u*(2)**(1/2))/pi)**(1/2)):
if (-u/2 <= x_f <= u/2) and (-u/2 <= x_f <= u/2):
```

Determine which alpha particles generate visible tracks

It is the final step, and the visible track determination is computed by using the rejection technique. The distance limits for each radioactive element and an incident angle greater than the one critical was adopted as conditions. However, these two conditions hardly depend on the etching process, expressed by the semi-empirical V-function (as Section 2.1).

```
if Rmin <= d_0H <= Rmax:
if i_angle >= c_angle:
register += 1
```

So the partial sensitivity, when sampling N alpha particle positions, is:

```
sensitivity = (register/N) * (h_cy*r_cy**2) / (2*u*(2)**(1/2))
```

Appendix B

Efficiency of a film covered SSNTD

An SSNTD can register alpha particles emitted by radon/thoron progeny or nuclear (n,α) reactions, using some films such as absorbers or converters, respectively. In both cases, the number of alpha particles, that travel through the film and reach the detector surface generating visible tracks, will allow to estimate the efficiency of a specific film covered detector (using some Python recipes). We can use standard SSNTDs such as the LR-115 or CR-39 covered by a film such as mylar, SN1 and others.

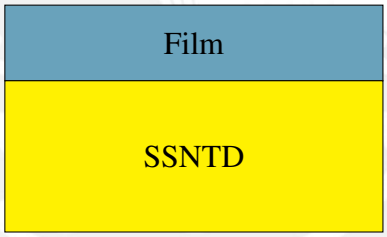

Calculation of the travel distance of alpha particles in a specific film

The stopping power $(-dE/dx)$ of alpha particle in a specific film (including its density) is given by SRIM 2013 program (http://www.srim.org). So the energy E_d of an alpha particle after travelling a distance d with initial energy E_i can be computed by solving the equation,

$$d = \int_{E_d}^{E_i} \frac{1}{\left(\frac{dE}{dx}\right)} dE \tag{B.1}$$

This equation can be solved in Python by interpolating $\frac{1}{\left(\frac{dE}{dx}\right)}$ using

```
interpolate.interp1d(x,y,'cubic')
```

then the integral is solved by

```
integrate.simps(y,x)
```

So we can calculate the distance d by using E_d, E_i and $(-dE/dx)$ for a specific film.

Alpha particles distribution on an absorber or in a converter

When using absorbers, alpha particles are distributed on the absorber surface and the distribution can be computed as follows:

```
x_2 = (-l/2) + (l * random.uniform(0,1))
y_2 = (-l/2) + (l * random.uniform(0,1))
z_2 =  (LR + H_ab) * random.uniform(0,1)
```

where l is the length and the width of the absorber, LR is the thickness of the SSNTD, and H_{ab} is the absorber's thickness.

When using converters, alpha particles are distributed in the converter because simulations in *MCNP*6.1.0 code only estimates the number of the alpha particles in the converter. So, we can compute the distribution of the alpha particles according to this simulation results.

```
x_3,y_2,z_3
```

How many alpha particles reach the detector surface

Herein, it is well known that the alpha particle is emitted isotropically. It can be computed by sampling random uniform directions for each alpha particle in spherical coordinates (θ_3, ϕ_2):

```
cos_theta_3 = -2 * random.uniform(0,1) + 1
phi_2 = 2 * pi * random.uniform(0,1)
```

Then, we can graphically simulate the process of reaching the detector surface by hitting an alpha particle from (x_2, y_2, z_2) with a polar angle θ_3, and azimuthal angle ϕ_2, along with the distance d, as shown as follows:

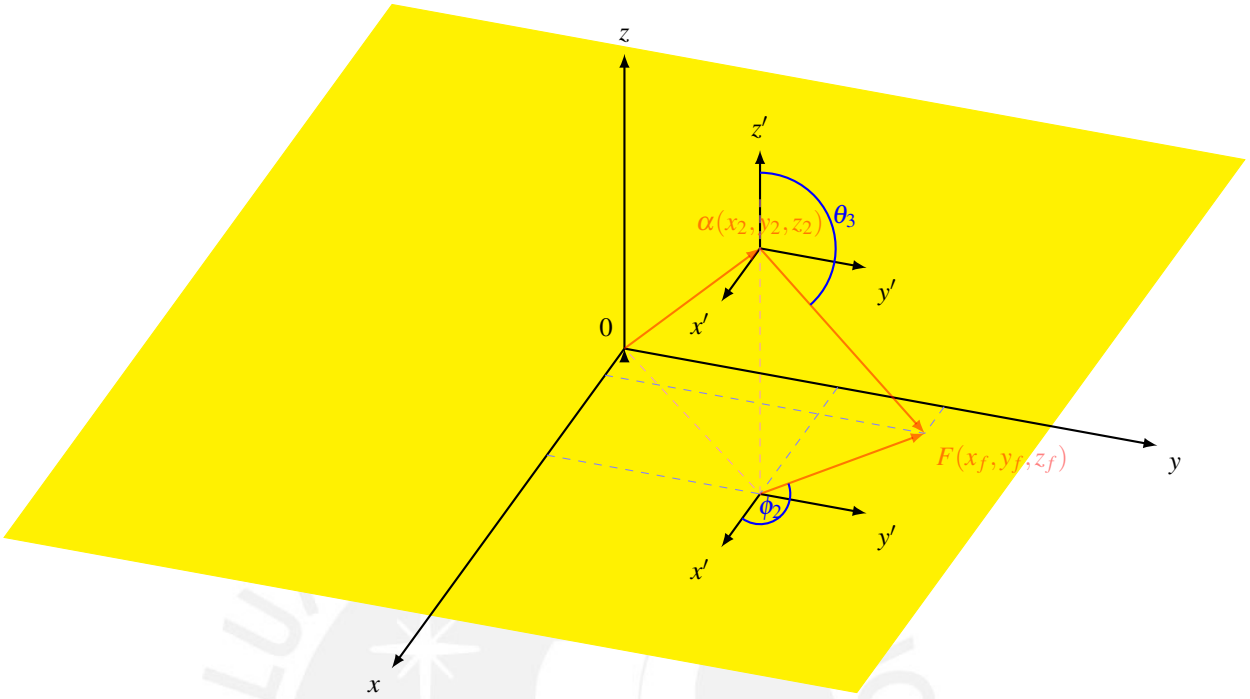

If an alpha particle with (x_f, y_f, z_f) final position is within the detector surface, we assume that this alpha particle reaches the detector. We also know that this alpha particle reaches the detector with an incident energy of E_d and an incident angle of $\phi_2 - \pi/2$.

Which alpha particles generate visible tracks?

Knowing the energy-angle curve $(E_{in}vs.\theta_{cric})$ for specific etching conditions, we easily select alpha particles with incident energies and angles within the curve.

```
angle_int = interpolate.interpd1(E_in,theta_circ,'cubic')
if (phi_3-pi/2) >= angle_int(E_d):
visible_track +=1
```

So the efficiency, when sampling N alpha particles positions in the film is:

```
efficiency = visible_track/N
```

Appendix C

Academic Achievements

Publications

1. **Pérez, B.**, López, M. E., & Palacios, D. (2021). Overlapping correction suitable for an LR-115 detector located inside a diffusion chamber. Radiation Physics and Chemistry, 109470.

2. **Pérez, B.**, López, M. E., & Palacios, D. (2021). Concentric rings formation on etched LR-115 in bare mode by unconventional exposition. Nuclear Instruments and Methods in Physics Research Section B: Beam Interactions with Materials and Atoms, 496, 37-44.

3. **Pérez, B.**, López, M. E., & Palacios, D. (2020). Theoretical and experimental study of the LR-115 detector response in a non-commercial radon monitor. Applied Radiation and Isotopes, 160, 109112.

4. Pereyra, P., Herrera, M. L., Palacios, D., Viloria, T., Vadillo, E., **Pérez, B.**, & Sajo-Bohus, L. (2020). Nuclear track detector response to energetic heavy ions: study case. Journal of Radioanalytical and Nuclear Chemistry, 1-6.

5. Lázaro, L. V., Herrera, M. E. L., Pereyra, P., Fernández, D. P., **Pérez, B.**, Rojas, J., & Sajo-Bohus, L. (2019). Measurement of radon in soils of Lima City-Peru during the period 2016-2017. Earth Sciences Research Journal, 23(3), 171-183.

6. Rojas, J., Palacios, D., Pereyra, P.,**Pérez, B.**, Bohus, L. S., & López, M. E. (2018). A semi-empirical approach to estimate the parameters determining the LR-115 detector response in radon measurements. Radiation Measurements, 118, 36-42.

Events

XX International Symposium on Solid State Dosimetry. December 2020. *"Estimation of CR-39 response to isotopic neutron source for neutron dosimetry applications"*
XI Congreso Regional de Seguridad Radiológica y Nuclear. April 2018, La Habana-Cuba. *"B.trαcks as a friendly computer program for simulating SSNTD sensitivity to radon and parameters of alpha particle registration in diffusion chambers"*

Stage

Mi.am s.rl. company and Universidad Politecnico di Milano. October 2018 to January 2019, Italy. *"Work and investigation collaborations in the simulation and radon measurements fields*.

Awards and Fundings

1. **Outstanding of the month**. June 2021, CONCyTEC - Peru. *Concentric rings formation on etched LR-115 in bare mode by unconventional exposition*
2. **Outstanding of the month**. June 2020, CONCyTEC - Peru. *Theoretical and experimental study of the LR-115 detector response in a non-commercial radon monitor*
3. **Doctoral Scholarship**. CONCyTEC $N° - 000236 - 2015 - FONDECYT$. August 2016 to July 2019.
4. **Master Scholarship**. Fund for FONDECYT 012-2013. April 2014 to December 2015.